CrossMark

J. Fluid Mech. (2016), *vol.* 793, *pp.* 709–748. © Cambridge University Press 2016
doi:10.1017/jfm.2016.137

Computations of equilibrium and non-equilibrium turbulent channel flows using a nested-LES approach

Yifeng Tang[1] **and Rayhaneh Akhavan**[1,†]

[1]Department of Mechanical Engineering, The University of Michigan, Ann Arbor, MI 48109-2125, USA

(Received 26 January 2015; revised 27 January 2016; accepted 14 February 2016;
first published online 22 March 2016)

A new nested-LES approach for computation of high Reynolds number, equilibrium, and non-equilibrium, wall-bounded turbulent flows is presented. The method couples coarse-resolution LES in the full computational domain with fine-resolution LES in a minimal flow unit to retain the accuracy of well-resolved LES throughout the computational domain, including in the near-wall region, while significantly reducing the computational cost. The two domains are coupled by renormalizing the instantaneous velocity fields in each domain dynamically during the course of the simulation to match the wall-normal profiles of single-time, ensemble-averaged kinetic energies of the components of 'mean' and fluctuating velocities in the inner layer to those of the minimal flow unit, and in the outer layer to those of the full domain. This simple renormalization procedure is shown to correct the energy spectra and wall shear stresses in both domains, thus leading to accurate turbulence statistics. The nested-LES approach has been applied to computation of equilibrium turbulent channel flow at $Re_\tau \approx 1000$, 2000, 5000, 10 000, and non-equilibrium, strained turbulent channel flow at $Re_\tau \approx 2000$. In both flows, nested-LES predicts the skin friction coefficient, first- and higher-order turbulence statistics, spectra and structure of the flow in agreement with available DNS and experimental data. Nested-LES can be applied to any flow with at least one direction of local or global homogeneity, while reducing the required number of grid points from $O(Re_\tau^2)$ of conventional LES to $O(\log Re_\tau)$ or $O(Re_\tau)$ in flows with two or one locally or globally homogeneous directions, respectively.

Key words: turbulent flows, turbulence modelling, turbulence simulation

1. Introduction

Large-eddy simulation (LES) is a method for predicting turbulent flows based on direct computation of the large, energy-containing scales of motion and modelling the effect of the small scales on the resolved scales. The recent years have witnessed many advances in LES techniques (Sagaut & Deck 2009). Nevertheless, computation of high Reynolds number, complex, wall-bounded turbulent flows continues to remain a challenge for LES. The bottleneck arises from the stringent resolution requirements

† Email address for correspondence: raa@umich.edu

https://doi.org/10.1017/jfm.2016.137 Published online by Cambridge University Press

of LES in the near-wall region, where the energy-containing eddies have a size proportional to their distance from the wall. Resolving these eddies in LES requires $O(Re_x^{1.8})$ grid points in turbulent boundary layers (Chapman 1979) or $O(Re_\tau^2)$ grid points in general wall-bounded flows (Jimenez 2003), where $Re_\tau \equiv u_\tau \delta/\nu$ denotes the friction Reynolds number, u_τ is the friction velocity, δ is the boundary layer thickness, channel half-height, or pipe radius and ν is the kinematic viscosity. These grid point requirements are not very different from the $O(Re_\tau^{9/4})$ grid points required in DNS (Jimenez 2003), and make the computation of high Reynolds number turbulent flows typical of engineering applications prohibitive.

A number of wall modelling approaches have been proposed over the years to bypass these stringent resolution requirements. These approaches can be broadly classified into two categories: approaches based on formulation of off-wall boundary conditions for either the shear stress or velocity analytically or empirically, and those based on numerical solution of alternative, simplified dynamical equations in the inner layer. In the first category, a set of approximate boundary conditions is specified at the first grid point away from the wall. These approximate boundary conditions can be derived either from simple algebraic equations which satisfy the law of the wall (Deardorff 1970; Schumann 1975) or from analytical integration of simplified momentum equations in the vicinity of the wall (Hoffmann & Benocci 1995; Chung & Pullin 2009), or from empirical correlations between the fluctuating velocities or the fluctuating velocities and shear stresses in the inner and outer layers (Mathis, Hutchins & Marusic 2011). In the second category, the flow in the inner layer is computed using simplified, less expensive dynamical equations, and the solutions are matched to the LES solution away from the wall. Commonly used examples of such equations are thin boundary layer Reynolds-averaged Navier–Stokes (RANS) equations (Balaras, Benocci & Piomelli 1996; Cabot & Moin 1999), unsteady RANS equations (Spalart *et al.* 1997; Nikitin *et al.* 2000; Menter & Egorov 2005; Shur *et al.* 2008), or certain lower-order forms of LES equations (Kemenov & Menon 2003).

Approximate off-wall boundary conditions can provide reasonable accuracy in simple, equilibrium, wall-bounded flows. However, in more complex flows, such as flows with mean three-dimensionality or separation, they become inaccurate (Piomelli 2008). Methods based on alternative dynamical equations in the inner layer often face the difficulty of exchanging information between two solutions with disparate spectral content, such as RANS and LES (Sagaut & Deck 2009). One well-known manifestation of this difficulty is the 'logarithmic layer mismatch' observed in many RANS/LES based models in equilibrium wall flows.

In this study, we propose an alternative approach for computing high Reynolds number wall-bounded turbulent flows based on nested-LES. In this approach, two simultaneous, nested, large-eddy simulations are performed; one in the full computational domain at coarse resolution, the other in a minimal flow unit at fine resolution. The LES solution in the minimal flow unit is used to dynamically 'correct' the full-domain LES in the inner layer, while the LES solution in the full domain is used to dynamically 'correct' the minimal-flow-unit LES in the outer layer. The method can be applied to any flow with at least one direction of 'global' or 'local' homogeneity, and retains the accuracy of well-resolved LES in both the near-wall and outer regions, while reducing the required number of grid points from $O(Re_\tau^2)$ of conventional LES to $O(\log Re_\tau)$ or $O(Re_\tau)$ in flows with two or one locally or globally homogeneous directions, respectively.

The organization of the paper is as follows. In § 2, the nested-LES approach is detailed. Section 3 reviews the numerical methods, simulation parameters and methods

https://doi.org/10.1017/jfm.2016.137 Published online by Cambridge University Press

for reconstruction of true RANS turbulence statistics employed in the present study. The performance of nested-LES in equilibrium turbulent channel flow at $Re_\tau \approx 1000$, 2000, 5000 and 10 000 is discussed in § 4, while § 5 reviews the performance of nested-LES in non-equilibrium, strained turbulent channel flow at $Re_\tau \approx 2000$. The computational savings offered by nested-LES are discussed in § 6. Section 7 presents a summary and conclusions.

2. The nested-LES approach

2.1. *Overview*

It has been recognized, since the pioneering work of Townsend (1958, 1976), that two classes of organized structures play a role in the dynamics of wall turbulence: small-scale, near-wall structures, whose size scales with the inner length scale, ν/u_τ; and large-scale, outer-layer structures, whose size scales with the outer length scale, δ. Earlier studies considered the outer-layer structures to be passive, with no substantial influence on the near-wall dynamics (Robinson 1991). This view has been challenged by more recent studies, which have shown an active role for both classes of structures (Balakumar & Adrian 2007), as well as a strong coupling between the two (Smits, McKeon & Marusic 2011). The outer-layer structures have been shown to strongly influence both the fluctuating velocity and pressure fields in the near-wall region (Hoyas & Jimenez 2006; Hutchins & Marusic 2007; Jimenez & Hoyas 2008; Mathis, Hutchins & Marusic 2009), and the Reynolds and wall shear stresses (Hutchins & Marusic 2007; Marusic & Heuer 2007). These interactions have been shown to become more pronounced as the Reynolds number increases (Smits *et al.* 2011). More recently, it has been proposed that the influence of large-scale structures on the near-wall structures is in the form of an amplitude modulation (Talluru *et al.* 2014). These results all point to a strong coupling between the near-wall and outer-layer structures.

From an LES standpoint, the turbulence dynamics in the outer layer can be computed using LES with a coarse-resolution, Reynolds-number-independent grid. This grid, however, becomes inadequate in the inner layer. The approach adopted in the present study to overcome this limitation is to perform two nested large-eddy simulations: one in the full domain at coarse-resolution, and the other in a minimal flow unit at fine resolution. The LES solution in the well-resolved minimal flow unit is then used to dynamically 'correct' the coarse-resolution, full-domain LES solution in the inner layer. A minimal flow unit is known to accurately predict the normalized turbulence statistics in the inner layer (Jimenez & Moin 1991; Flores & Jimenez 2010). However, it cannot accurately predict the wall shear stresses in the absence of proper outer-layer structures (Flores & Jimenez 2010; Hwang 2013). To remedy this problem, the outer-layer solution in the minimal flow unit also needs to be 'corrected' based on the solution in the full-domain LES. Thus, a two-way coupling between the two domains is required, in which the LES solution in the minimal flow unit is used to dynamically 'correct' the full-domain LES in the inner layer, while the LES solution in the full domain is used to dynamically 'correct' the minimal-flow-unit LES in the outer layer.

In the nested-LES approach, this 'correction' and coupling between the two domains is achieved by renormalizing the instantaneous LES velocity fields in both domains dynamically during the course of the simulation to match the wall-normal profiles of single-time ensemble-averaged kinetic energies of components of the 'mean' and fluctuating velocities in both domains to those of the minimal flow unit in the inner

https://doi.org/10.1017/jfm.2016.137 Published online by Cambridge University Press

layer, and to those of the full domain in the outer layer. It will be shown in § 4 that this simple renormalization is sufficient to correct the wall shear stresses and energy spectra in both domains, thus leading to accurate turbulence statistics. Given the definition of a minimal flow unit, application of the nested-LES approach requires flows which are 'locally' or 'globally' homogeneous in at least one wall-parallel direction.

2.2. *Implementation*

The nested-LES approach is based on the solution of LES equations at coarse resolution in the full domain, coupled with well-resolved LES in a minimal flow unit. For incompressible flow, the LES equations are given by (Sagaut & Meneveau 2006)

$$\frac{\partial \overline{u}_i}{\partial t} + \frac{\partial}{\partial x_j}(\overline{u_i u_j}) = -\frac{1}{\rho}\frac{\partial \overline{p}}{\partial x_i} + \nu \frac{\partial^2 \overline{u}_i}{\partial x_j^2}; \quad \frac{\partial \overline{u}_i}{\partial x_i} = 0, \tag{2.1a,b}$$

where the overbar denotes a filter which removes the small scales, $\overline{u}_i$ is the velocity field resolved in LES, $\overline{p}$ is the resolved pressure field, ρ is the density and ν is the kinematic viscosity. The term $\overline{u_i u_j}$ includes the effect of the subgrid scales on the resolved scales, and needs to be modelled.

To proceed with the nested-LES approach, let $\overline{u}_{\alpha,\mathscr{D}}(\boldsymbol{x}, t)$ denote the LES velocity fields in the full domain and minimal flow unit of nested-LES at the conclusion of time step t, with $\mathscr{D} = \mathscr{F}$ denoting the full domain, and $\mathscr{D} = \mathscr{M}$ denoting the minimal flow unit. The key to the nested-LES approach is a renormalization procedure in between time steps t and $t + \mathrm{d}t$, in which the velocity fields, $\overline{u}_{\alpha,\mathscr{D}}(\boldsymbol{x}, t)$, in both domains are 'renormalized' to $\overline{u}^R_{\alpha,\mathscr{D}}(\boldsymbol{x}, t)$. The LES solution at $t + \mathrm{d}t$ in each domain is then advanced using $\overline{u}^R_{\alpha,\mathscr{D}}(\boldsymbol{x}, t)$ instead of $\overline{u}_{\alpha,\mathscr{D}}(\boldsymbol{x}, t)$. To construct the renormalized velocity fields, $\overline{u}^R_{\alpha,\mathscr{D}}(\boldsymbol{x}, t)$, the velocity field, $\overline{u}_{\alpha,\mathscr{D}}(\boldsymbol{x}, t)$, in each domain is decomposed as

$$\overline{u}_{\alpha,\mathscr{D}}(\boldsymbol{x}, t) = \langle\langle \overline{u}_{\alpha,\mathscr{D}}(\boldsymbol{x}, t)\rangle\rangle + \overline{u}''_{\alpha,\mathscr{D}}(\boldsymbol{x}, t), \tag{2.2}$$

where $\langle\langle\ \rangle\rangle$ denotes a single-time ensemble-average over the locally or globally homogeneous wall-parallel flow directions, and $\langle\langle \overline{u}_{\alpha,\mathscr{D}}(\boldsymbol{x}, t)\rangle\rangle$ and $\overline{u}''_{\alpha,\mathscr{D}}(\boldsymbol{x}, t)$ are the single-time 'mean' and fluctuating parts of the original velocity field, respectively. The renormalized velocity field, $\overline{u}^R_{\alpha,\mathscr{D}}(\boldsymbol{x}, t)$, in each domain is then defined as

$$\overline{u}^R_{\alpha,\mathscr{D}}(\boldsymbol{x}, t) = \langle\langle \overline{u}_{\alpha,\mathscr{D}}(\boldsymbol{x}, t)\rangle\rangle R(\langle\langle \overline{u}_{\alpha,\mathscr{D}}\rangle\rangle \langle\langle \overline{u}_{\alpha,\mathscr{D}}\rangle\rangle) + \overline{u}''_{\alpha,\mathscr{D}}(\boldsymbol{x}, t) R(\langle\langle \overline{u}''_{\alpha,\mathscr{D}} \overline{u}''_{\alpha,\mathscr{D}}\rangle\rangle), \tag{2.3}$$

where $R(\phi_{\alpha,\mathscr{D}})$ are renormalization functions, given by

$$R(\phi_{\alpha,\mathscr{D}}) = (\phi_{\alpha,\mathscr{M}}/\phi_{\alpha,\mathscr{D}})^{1/2}, \quad \text{at } z \leqslant z^*, \tag{2.4a}$$

$$R(\phi_{\alpha,\mathscr{D}}) = (\phi_{\alpha,\mathscr{F}}/\phi_{\alpha,\mathscr{D}})^{1/2}, \quad \text{at } z > z^*, \tag{2.4b}$$

where $\phi_{\alpha,\mathscr{D}}$ can denote $\langle\langle \overline{u}_{\alpha,\mathscr{D}}\rangle\rangle \langle\langle \overline{u}_{\alpha,\mathscr{D}}\rangle\rangle$ or $\langle\langle \overline{u}''_{\alpha,\mathscr{D}} \overline{u}''_{\alpha,\mathscr{D}}\rangle\rangle$ with no summation implied over the index α. Equations (2.4*a*) and (2.4*b*) indicate that the renormalization functions in the full domain assume a value different from unity, $R(\phi_{\alpha,\mathscr{F}}) \neq 1$, only for $z \leqslant z^*$, while those in the minimal flow unit assume a value different from unity, $R(\phi_{\alpha,\mathscr{M}}) \neq 1$, only for $z > z^*$.

The renormalization procedures described by (2.2)–(2.4) rescale the velocity fields in the full domain and the minimal flow unit to match the wall-normal profiles of the single-time ensemble-averaged kinetic energies of the components of the 'mean'

https://doi.org/10.1017/jfm.2016.137 Published online by Cambridge University Press

velocity, $\langle\langle\overline{u}_\alpha\rangle\rangle\langle\langle\overline{u}_\alpha\rangle\rangle$, and the fluctuating velocity, $\langle\langle\overline{u}''_\alpha\overline{u}''_\alpha\rangle\rangle$, in both domains to those of the minimal flow unit in the inner layer, $z \leqslant z^*$, and to those of the full domain in the outer layer, $z > z^*$.

The fundamental principle behind the renormalization procedures of (2.2)–(2.4) is the concept of energy cascade. At $z > z^*$, the minimal flow unit is not large enough to accommodate the large-scale, outer-layer turbulence structures. If it did, however, the amount of turbulence kinetic energy (TKE) in each component of the fluctuating velocity which would cascade down to the scales that are contained within the minimal flow unit would be the energy that exists in the corresponding fluctuating velocity component in the large domain. This implies that for $z > z^*$, the magnitude of $\langle\langle\overline{u}''_\alpha\overline{u}''_\alpha\rangle\rangle$ in the minimal flow unit should be dictated by that in the full domain for each velocity component, α. In these arguments, the viscous dissipation of TKE in the energy containing and equilibrium range eddies in both domains have been neglected, and it is assumed that the largest scales of the minimal flow unit fall somewhere within the universal equilibrium range. Similarly, for $z < z^*$, where the full domain does not have sufficient resolution to resolve the near-wall eddies, the proper amount of energy $\langle\langle\overline{u}''_\alpha\overline{u}''_\alpha\rangle\rangle$ which should reside in each component of TKE in the full domain is that which exists in the corresponding α component of the fluctuating velocity in the minimal flow unit. For the above arguments to be valid, both domains need to have the same mean velocity profiles and wall shear stresses. This is ensured by equating the kinetic energies of the components of the mean velocity, $\langle\langle\overline{u}_\alpha\rangle\rangle\langle\langle\overline{u}_\alpha\rangle\rangle$, in both domains to that of the full domain for $z > z^*$, and to that of the minimal flow unit for $z \leqslant z^*$.

While the renormalization procedures of (2.2)–(2.4) are designed to correct only the areas under the spectra curves in each domain, in practice we find that this simple renormalization procedure also corrects the shapes of the spectra in both domains, thus ensuring that not only the flow statistics up to second order, but also all higher-order turbulence statistics, are correctly predicted by the nested-LES approach. These results are discussed in detail in § 4.

The location z^* in (2.4) represents the wall-normal position at which the basis for renormalization of the velocity fields is switched from the LES solution in the minimal flow unit at $z \leqslant z^*$ to the LES solution in the full domain at $z > z^*$. The value of z^* is chosen to place z^* in the overlap region between the inner layer, $z/\delta < 0.1$ (Pope 2000, table 7.1), and outer layer, $z^+ > 50$ (Pope 2000, table 7.1). Accordingly, a value of $z^*/\delta = 0.05$ has been used in all the simulations reported in this study. However, the results were found to be fairly insensitive to the exact choice of z^* for $0.04 \leqslant z^*/\delta \leqslant 0.06$. A detailed discussion of the effect of z^* on the predictions of nested-LES is given in § 4.5.

In practice, the renormalization functions, $R(\phi_{\alpha,\mathscr{D}})$, remain fairly close to unity throughout $0.0 \leqslant z/\delta \leqslant 1$, and confined to 1 ± 0.001 for $0.05 \leqslant z/\delta < 1$ (see §§ 4.6 and 5.3). With a choice of $z^*/\delta = 0.05$ and these values of $R(\phi_{\alpha,\mathscr{D}})$, no significant jump discontinuity occurs at $z = z^*$ when the solution in each domain is switched from its original velocity field, $\overline{u}_{\alpha,\mathscr{D}}(\boldsymbol{x}, t)$, to the renormalized velocity field, $\overline{u}^R_{\alpha,\mathscr{D}}(\boldsymbol{x}, t)$. One could also introduce a blending zone, in which the renormalized and original velocity fields in each domain are gradually blended together. However, we found no particular advantage to introducing such a blending zone, and adopted the simpler approach of switching between the renormalized and original velocity fields at z^*.

After application of the renormalization procedure (2.2)–(2.4), the velocity fields, $\overline{u}^R_{\alpha,\mathscr{D}}(\boldsymbol{x}, t)$, are no longer divergence free. However, one should note that $\overline{u}^R_{\alpha,\mathscr{D}}(\boldsymbol{x}, t)$ represent only intermediate velocity fields in between time steps. By the end of

https://doi.org/10.1017/jfm.2016.137 Published online by Cambridge University Press

each time step, the velocity field in each domain is once again projected onto the divergence-free space as part of the solution for that time step. These divergence-free velocity fields no longer have identical turbulence statistics in the two domains, with the difference between the two sets of statistics being equal to the values of $R(\phi_{\alpha,\mathscr{D}})$ which need to be applied at the next time step. All the mean velocities and LES turbulence intensities reported in the present study were obtained from the divergence-free velocity fields at the conclusion of each time step in the full domain.

3. Application to equilibrium and non-equilibrium turbulent channel flows

The nested-LES approach has been applied to LES of equilibrium turbulent channel flow at $Re_\tau \approx 1000$, 2000, 5000 and 10 000, and non-equilibrium, strained turbulent channel flow at $Re_\tau \approx 2000$. This section describes the numerical methods, simulation parameters, choice of subgrid-scale (SGS) model and reconstruction of RANS statistics employed in these studies.

3.1. *Numerical methods*

The LES equations (2.1) were solved in the full domain and the minimal flow unit using a patching collocation spectral domain-decomposition method, employing Fourier series in the streamwise (x) and spanwise (y) directions, and mapped Chebyshev polynomials in the wall-normal (z) direction (Orszag 1980; Canuto *et al.* 1988). A schematic of the channel and the coordinate system is shown in figure 1(*a*). Note that no specific positioning of the minimal flow unit relative to the full domain is required in the nested-LES approach, as the two domains are coupled only through their single-time-averaged turbulence statistics. The computational box spans the full height of the channel, from one wall to the other, in both the full domain and the minimal flow unit, and is partitioned into three non-overlapping sub-domains Ω_s ($s = 1, 2, 3$) in the wall-normal direction, as shown in figure 1(*b*). This partitioning allows the grid-point distribution in each zone to be customized to minimize the required number of grid points in the wall-normal direction. The same internal interface locations and wall-normal distribution of grid points were employed in the full domain and the minimal flow unit at each Reynolds number, with the internal interface locations between the Ω_2/Ω_1 or Ω_2/Ω_3 sub-domains placed at $z^+ \approx 200$–250 at all Reynolds numbers, as shown in table 1, where the $+$ superscript denotes normalization using inner variables. The continuity of the velocity field, $\overline{u}_i$, and its normal derivative, $\partial\overline{u}_i/\partial z$, were enforced at the internal interfaces between these sub-domains, resulting in solutions which are C^1 continuous (Canuto *et al.* 1988).

Algebraic mappings (Kosloff & Talezer 1993) were used to project the $\xi_s \in [-1, 1]$ domain of Chebyshev polynomials to the physical domain in the wall-normal direction, in order to maintain the desired distribution of grid points in each sub-domain. The specific algebraic mappings employed in the present study are given by

$$\frac{z}{h} = \left(\frac{L_{z,s}}{h} - 1\right) - \frac{A_w(1-\xi_s)}{1 + 2A_w h/L_{z,s} + \xi_s} \quad \text{for } s = 1, \tag{3.1}$$

$$\frac{z}{h} = \frac{A_c \xi_s}{(1 + (2A_c h/L_{z,s})^2 - \xi_s^2)^{1/2}} \quad \text{for } s = 2, \tag{3.2}$$

$$\frac{z}{h} = -\left(\frac{L_{z,s}}{h} - 1\right) + \frac{A_w(1-\xi_s)}{1 + 2A_w h/L_{z,s} + \xi_s} \quad \text{for } s = 3, \tag{3.3}$$

https://doi.org/10.1017/jfm.2016.137 Published online by Cambridge University Press

https://doi.org/10.1017/jfm.2016.137 Published online by Cambridge University Press

$Re_\tau\|_{nom}$	$\mathscr{D}$	$(L_x, L_y, L_{z,s})/h$	$(L_x^+, L_y^+, L_{z,s}^+)\|_{nom}$	$N_x,\ N_y,\ N_{z,s}$	$\Delta_x^+,\ \Delta_y^+$	A_w	A_c
Nested-LES in equilibrium turbulent channel flow							
1000	$\mathscr{F}$	$2\pi,\ \pi,\ 0.2/1.6/0.2$	6280, 3140, 200/1600/200	64, 64, 17/33/17	98, 49	0.1	1.2
	$\mathscr{M}$	$\pi,\ \pi/2,\ 0.2/1.6/0.2$	3140, 1570, 200/1600/200	64, 64, 17/33/17	49, 25		
2000	$\mathscr{F}$	$2\pi,\ \pi,\ 0.1/1.8/0.1$	12 560, 6280, 200/3600/200	64, 64, 17/33/17	196, 98	0.05	1.5
	$\mathscr{M}$	$\pi/2,\ \pi/4,\ 0.1/1.8/0.1$	3140, 1570, 200/3600/200	64, 64, 17/33/17	49, 25		
5000	$\mathscr{F}$	$2\pi,\ \pi,\ 0.05/1.9/0.05$	31 400, 15 700, 250/9500/250	64, 64, 17/33/17	490, 245	0.02	2.5
	$\mathscr{M}$	$\pi/4,\ \pi/8,\ 0.05/1.9/0.05$	3920, 1960, 250/9500/250	64, 64, 17/33/17	61, 31		
10 000	$\mathscr{F}$	$2\pi,\ \pi,\ 0.025/1.95/0.025$	62 800, 31 400, 250/19 500/250	64, 64, 17/33/17	980, 490	0.008	2.5
	$\mathscr{M}$	$\pi/8,\ \pi/16,\ 0.025/1.95/0.025$	3920, 1960, 250/19 500/250	64, 64, 17/33/17	61, 31		
2000^h	$\mathscr{F}$	$2\pi,\ \pi,\ 0.1/1.8/0.1$	12 560, 6280, 200/3600/200	128, 128, 33/65/33	98, 49	0.05	1.5
	$\mathscr{M}$	$\pi/2,\ \pi/4,\ 0.1/1.8/0.1$	3140, 1570, 200/3600/200	128, 128, 33/65/33	25, 12		
5000^h	$\mathscr{F}$	$2\pi,\ \pi,\ 0.05/1.9/0.05$	31 400, 15 700, 250/9500/250	128, 128, 33/65/33	245, 123	0.02	2.5
	$\mathscr{M}$	$\pi/4,\ \pi/8,\ 0.05/1.9/0.05$	3920, 1960, 250/9500/250	128, 128, 33/65/33	31, 15		
Non-nested LES in equilibrium turbulent channel flow							
2000^F	$\mathscr{F}$	$2\pi,\ \pi,\ 0.1/1.8/0.1$	12 560, 6280, 200/3600/200	64, 64, 17/33/17	196, 98	0.05	1.5
2000^M	$\mathscr{M}$	$\pi/2,\ \pi/4,\ 0.1/1.8/0.1$	3140, 1570, 200/3600/200	64, 64, 17/33/17	49, 25	0.05	1.5
$2000^{F,h}$	$\mathscr{F}$	$2\pi,\ \pi,\ 2$	12 560, 6280, 4000	256, 256, 257	49, 25	—	—
Nested-LES in non-equilibrium, strained turbulent channel flow							
2000-S	$\mathscr{F}$	$2\pi,\ \pi,\ 0.1/1.8/0.1$	12 560, 6280, 200/3600/200	64, 64, 17/33/17	196, 98	0.05	1.5
	$\mathscr{M}$	$\pi/2,\ \pi/4,\ 0.1/1.8/0.1$	3140, 1570, 200/3600/200	64, 64, 17/33/17	49, 25		
Non-nested LES in non-equilibrium, strained turbulent channel flow							
2000-S^F	$\mathscr{F}$	$2\pi,\ \pi,\ 0.1/1.8/0.1$	12 560, 6280, 200/3600/200	64, 64, 17/33/17	196, 98	0.05	1.5
2000-S^M	$\mathscr{M}$	$\pi/2,\ \pi/4,\ 0.1/1.8/0.1$	3140, 1570, 200/3600/200	64, 64, 17/33/17	49, 25	0.05	1.5

TABLE 1. Computational domain sizes, grid resolutions, grid spacings and mapping parameters employed in nested-LES and non-nested LES of equilibrium and non-equilibrium turbulent channel flow in the present study.

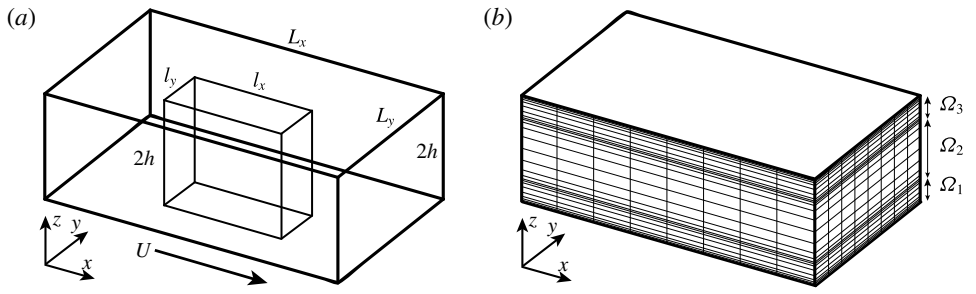


FIGURE 1. (*a*) The computational domains and coordinate system employed in nested-LES of equilibrium and non-equilibrium turbulent channel flows: ——, full domain; ——, minimal flow unit; (*b*) the patching collocation sub-domains and wall-normal grid distribution employed in both the full domain and minimal flow unit of nested-LES.

where h denotes the channel half-height, $L_{z,s}$ denotes the wall-normal height of sub-domain Ω_s and A_w and A_c are appropriate scale factors. The specific values of $L_{z,s}$, A_w, and A_c for each case are summarized in table 1.

Using the mappings (3.1)–(3.3), nearly the same distribution of grid points in inner scaling (+ units) was maintained in the Ω_1 and Ω_3 sub-domains, with a fixed number of grid points, at all Reynolds numbers, as shown in table 2. Maintaining such a distribution of grid points in the Ω_1 and Ω_3 sub-domains was found to be critical for accurate prediction of the friction coefficient at all Reynolds numbers. Similarly, in the wake region, $z/h > 0.3$, the mappings result in a nearly uniform distribution of grid points in outer (z/h) scaling at all Reynolds numbers, as shown in table 2. This makes the required number of grid points in the wake region also independent of Reynolds number for a full domain of a fixed size in outer scaling. In the logarithmic region ($z^+ > 3Re_\tau{}^{1/2}$ and $z/h < 0.3$) (Marusic *et al.* 2013; Meneveau & Marusic 2013), where the size of the eddies grows in proportion to the distance from the wall, the required number of grid points has a weak dependence on Re_τ, and grows as $\log(Re_\tau)$, as shown in § 6. Because of the weak, logarithmic, nature of this dependence on Re_τ, computations can be performed with a fixed number of grid points in the wall-normal direction over nearly a decade of Re_τ values in this region as well, which is the approach adopted in the present study. With such a distribution of grid points, the near-wall region is well resolved in both the minimal flow unit and the full domain, and both domains can be solved subject to the no-slip boundary conditions at the walls, without the need for any wall models.

The LES governing equations were integrated in time using a second-order fractional-step method, with explicit treatment of the nonlinear terms using an Adams–Bashforth scheme, and semi-implicit treatment of the pressure–viscous terms using a Crank–Nicolson scheme (Yakhot *et al.* 1989). All the simulations were de-aliased using the so-called 2/3 rule (Canuto *et al.* 1988), and were initialized from an LES database of a fully developed turbulent channel flow at $Re_\tau \approx 570$. A constant flow rate (per unit width) was maintained in both the full domain and minimal flow unit throughout the course of all simulations.

3.2. *Simulation parameters*

The simulations of equilibrium turbulent channel flow were performed at bulk Reynolds numbers, $Re_b \equiv U_b h/\nu$, of 20 000, 45 000, 125 000 and 275 000, correspond-

https://doi.org/10.1017/jfm.2016.137 Published online by Cambridge University Press

$Re_\tau \approx 1000$		$Re_\tau \approx 2000$		$Re_\tau \approx 5000$		$Re_\tau \approx 10\,000$	
z/h	z^+	z/h	z^+	z/h	z^+	z/h	z^+
0.00000	0.00	0.00000	0.00	0.00000	0.00	0.00000	0.00
0.00064	0.64	0.00032	0.64	0.00014	0.69	0.00006	0.59
0.00260	2.60	0.00130	2.60	0.00056	2.79	0.00024	2.38
0.00595	5.95	0.00298	5.95	0.00128	6.40	0.00055	5.46
0.01082	10.82	0.00541	10.82	0.00234	11.68	0.00100	9.98
0.01739	17.39	0.00870	17.39	0.00377	18.87	0.00162	16.19
0.02591	25.91	0.01295	25.91	0.00566	28.28	0.00244	24.42
0.03667	36.67	0.01833	36.67	0.00807	40.34	0.00351	35.09
0.05000	50.00	0.02500	50.00	0.01111	55.56	0.00488	48.78
0.06621	66.21	0.03311	66.21	0.01489	74.46	0.00662	66.17
0.08549	85.49	0.04275	85.49	0.01951	97.56	0.00880	87.98
0.10769	107.69	0.05385	107.69	0.02500	125.00	0.01148	114.76
0.13204	132.04	0.06602	132.04	0.03124	156.20	0.01464	146.39
0.15673	156.73	0.07837	156.73	0.03782	189.10	0.01812	181.21
0.17878	178.78	0.08939	178.78	0.04392	219.59	0.02149	214.92
0.19434	194.34	0.09717	194.34	0.04836	241.79	0.02404	240.38
0.20000	200.00	0.10000	200.00	0.05000	250.00	0.02500	250.00
0.20000	200.00	0.10000	200.00	0.05000	250.00	0.02500	250.00
0.20555	205.55	0.10588	211.76	0.05523	276.15	0.03040	304.03
0.22193	221.93	0.12328	246.56	0.07080	354.02	0.04649	464.90
0.24839	248.39	0.15153	303.05	0.09639	481.94	0.07291	729.05
0.28384	283.84	0.18960	379.19	0.13145	657.25	0.10909	1 090.85
0.32692	326.92	0.23623	472.47	0.17530	876.51	0.15430	1 543.00
0.37623	376.23	0.29008	580.16	0.22714	1135.70	0.20770	2 077.02
0.43044	430.44	0.34980	699.60	0.28609	1430.46	0.26837	2 683.75
0.48832	488.32	0.41415	828.30	0.35126	1756.30	0.33538	3 353.80
0.54887	548.87	0.48204	964.09	0.42176	2108.79	0.40779	4 077.93
0.61127	611.27	0.55257	1105.15	0.49673	2483.66	0.48473	4 847.33
0.67491	674.91	0.62501	1250.01	0.57538	2876.92	0.56538	5 653.78
0.73933	739.33	0.69877	1397.54	0.65698	3284.88	0.64897	6 489.75
0.80422	804.22	0.77343	1546.87	0.74083	3704.16	0.73484	7 348.37
0.86937	869.37	0.84868	1697.35	0.82633	4131.67	0.82234	8 223.40
0.93466	934.66	0.92426	1848.52	0.91290	4564.52	0.91091	9 109.08
1.00000	1000.00	1.00000	2000.00	1.00000	5000.00	1.00000	10 000.00

TABLE 2. Wall-normal grid distribution employed in nested-LES and non-nested LES of equilibrium and non-equilibrium turbulent channel flow at $Re_\tau \approx 1000$, 2000, 5000 and 10 000 at 'standard' resolution.

ing to friction Reynolds numbers, $Re_\tau \equiv u_\tau h/\nu$, of 1016, 2066, 5051 and 10 068, respectively, based on the u_τ from Dean's correlation (Dean 1978). Throughout this study, these cases will be referred to as 'nominal' $Re_\tau \approx 1000$, 2000, 5000 and 10 000, respectively, as shown in table 1.

The simulations of non-equilibrium, strained turbulent channel flow were designed to emulate the experimental conditions of Driver & Hebbar (1991), in which an initially two-dimensional turbulent boundary layer (TBL) at $Re_\theta \approx 6900$ ($Re_\tau \approx 2000$) was driven to three-dimensionality by impulsive transverse motion of the wall at speed $V_s = U_\infty$ over a length $L_s \approx 32.6\delta_0$, followed by cessation of the transverse motion of

https://doi.org/10.1017/jfm.2016.137 Published online by Cambridge University Press

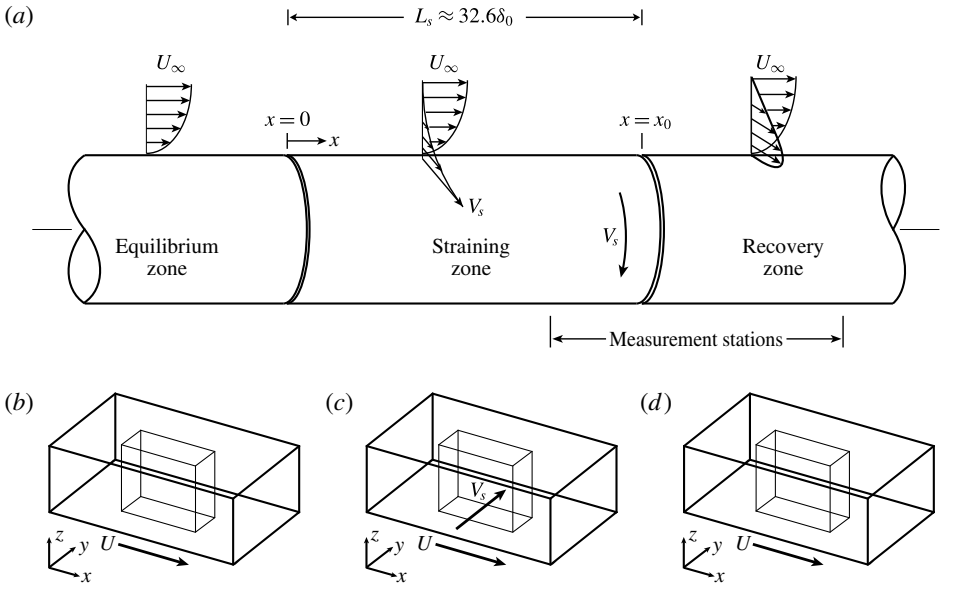


FIGURE 2. (*a*) Schematic of the experimental set-up of shear driven, three-dimensional turbulent boundary layer by Driver & Hebbar (1991); (*b–d*) schematic of the channel flows used in nested-LES of non-equilibrium, strained channel flow in each of the equilibrium, straining and recovery zones in the present study.

the wall, and recovery to initial two-dimensional state, as shown in figure 2(*a*). Here, U_∞ denotes the free-stream velocity in the original TBL, δ_0 denotes the boundary layer thickness at the end of the shearing zone and L_s denotes the length of the shearing zone. In the large-eddy simulations, a fully developed, equilibrium turbulent channel flow at $Re_\tau \approx 2000$ is subjected to impulsive transverse motion of one of the walls at speed $V_s = U_c$ for a time period T_s, followed by cessation of the transverse motion of the wall, and recovery to equilibrium turbulent channel flow, where U_c denotes the mean centreline velocity in the initial equilibrium turbulent channel. The correspondence between 'time' in the simulations and 'position' in the experiments was computed based on Taylor's hypothesis,

$$\frac{tU_c}{h} = \frac{x}{\delta(x)}, \tag{3.4}$$

where t is the time from the start of the transverse motion of the lower wall in the simulations, x denotes the streamwise distance from the leading edge of the moving wall section in the experiments (see figure 2*a*) and $\delta(x)$ is the local boundary thickness in the experiments. The evolution of turbulence statistics from equilibrium channel flow to strained, non-equilibrium flow, and recovery back to equilibrium turbulent channel flow was tracked in LES and compared to experimental measurements (Driver & Hebbar 1991). In comparing the turbulence statistics from TBL experiments to LES predictions in turbulent channel flow, the normalized wall-normal location, $z/\delta(x)$, mean velocities, $\langle\overline{u}_i\rangle/U_\infty$ and turbulent stresses, $\langle u_i' u_j'\rangle/U_\infty^2$, from the TBL were equated with z/h, $\langle\overline{u}_i\rangle/U_c$, and $\langle u_i' u_j'\rangle/U_c^2$ in channel flow, respectively.

https://doi.org/10.1017/jfm.2016.137 Published online by Cambridge University Press

All the simulations of equilibrium and non-equilibrium channel flow were performed in full domains of size $L_x \times L_y \times L_z = 2\pi h \times \pi h \times 2h$, and minimal flow units of size $l_x^+ \approx 3200$–3900, $l_y^+ \approx 1600$–1950, and $l_z = 2h$, in the streamwise, spanwise and wall-normal directions, respectively, as shown in table 1. The size of the minimal flow unit in the homogeneous flow directions was chosen to accommodate ∼3–4 near-wall structures in the streamwise, and ∼15–20 near-wall structures in the spanwise directions, to provide a reasonably adequate ensemble for the single-time averages employed in the decomposition and renormalization procedures of (2.2)–(2.4). Grid resolutions of $64 \times 64 \times 17/33/17$ were employed in both the full domain and the minimal flow unit as the standard resolution in all the simulations, independent of the Reynolds number. With these domains sizes and grid resolutions, grid spacings of $\Delta_x^+ \approx 50$–60 in the streamwise and $\Delta_y^+ \approx 25$–30 in the spanwise direction are maintained in the minimal flow unit at all Reynolds numbers, while in the full domain, grid spacings of $\Delta_x/h = 2\pi/64 \approx 0.1$ in the streamwise and $\Delta_y/h = \pi/64 \approx 0.05$ in the spanwise direction are maintained at all Reynolds numbers. In the wall-normal direction, the same grid distribution is used in the full domain and minimal flow unit at each Reynolds number. The specific grid distributions employed at each Reynolds number are shown in table 2. With the aid of the patching collocation method and the mappings discussed in § 3.1, a nearly fixed distribution of grid points in inner scaling (+ units) is maintained in the near-wall region ($0 \leqslant z^+ \leqslant 200$–$250$) at all Reynolds numbers to resolve the near-wall region down to the viscous sublayer and the wall, as shown in table 2. In the wake region, $z/h > 0.3$, the patching collocation method and the mappings discussed in § 3.1 result in nearly uniform grid spacings of $\Delta_z/h \approx 0.05$–0.1 at all Reynolds numbers, while in the logarithmic region, between $z^+ \geqslant 3Re_\tau^{1/2}$ and $z/h \leqslant 0.3$, the grid size almost linearly increases from its value in the near-wall sub-domain to its values in the wake region.

In addition to these 'standard resolution' cases, nested-LES of equilibrium turbulent channel flow at $Re_\tau \approx 2000$ and 5000 were performed with double the resolution in each direction, to verify the grid independence of the results. These cases, which were performed with grid resolutions of $128 \times 128 \times 33/65/33$, are denoted by cases 2000^h and 5000^h in table 1.

Furthermore, to assess the effectiveness of the nested-LES approach, a set of non-nested large-eddy simulations were performed in equilibrium and non-equilibrium turbulent channel flows at $Re_\tau \approx 2000$ in domains of the same size as the full domain and minimal flow unit of the nested-LES, with the same grid resolutions as those employed in nested-LES. These cases are denoted by 2000^F, 2000^M, 2000-S^F, 2000-S^M in table 1, representing non-nested equilibrium channel flow in the full domain, non-nested equilibrium channel flow in the minimal flow unit, non-nested sheared channel flow in the full domain and non-nested sheared channel flow in the minimal flow unit, respectively.

The turbulence statistics reported in equilibrium turbulent channel flow were obtained by ensemble averaging the flow quantities in space, over the homogeneous flow directions, and in time, over approximately ten eddy turnover times, h/u_τ. The turbulence statistics reported in the non-equilibrium, strained turbulent channel flow were obtained by ensemble averaging the flow quantities in space, over the homogeneous flow directions and over ten independent realizations of the strained turbulent channel flow, each initialized from a different nested-LES realization of a fully developed, equilibrium turbulent channel flow at $Re_\tau \approx 2000$.

https://doi.org/10.1017/jfm.2016.137 Published online by Cambridge University Press

3.3. *SGS model and reconstruction of RANS turbulence statistics*

The conventional approach to modelling the term $\overline{u_i u_j}$ in (2.1) is to represent it as $\overline{u_i u_j} = \overline{u}_i \overline{u}_j + \tau_{ij}$, and model the subgrid-scale stress tensor, $\tau_{ij} \equiv \overline{u_i u_j} - \overline{u}_i \overline{u}_j$ (Sagaut & Meneveau 2006). This choice, however, is not unique, and some investigators have favoured representing $\overline{u_i u_j}$ as $\overline{u_i u_j} = \overline{\overline{u}_i \overline{u}_j} + \overline{A}_{ij}$ and modelling $\overline{A}_{ij}$ (Winckelmans, Jeanmart & Carati 2002) or even modelling $\overline{u_i u_j}$ directly (Haliloglu & Akhavan 2004). The implementation of the nested-LES approach is independent of all such modelling issues. Nested-LES can be applied with any formulation of $\overline{u_i u_j}$, and any SGS model of choice.

In this study, the conventional definition of SGS stress, along with the dynamic Smagorinsky model (DSM) of Germano *et al.* (1991) and Lilly (1992) with sharp, spectral, cutoff filters has been used, because of its known performance characteristics and simplicity. Following the original formulation of Germano *et al.* (1991) and Lilly (1992), the implicit spectral cutoff LES filters were placed at the de-aliased grid filter location. Test filtering was applied only in the streamwise and spanwise directions, and the test filters were placed at half the implicit LES filter locations.

In LES, only the filtered velocity, $\overline{u}_i$, is computed. Consequently, the turbulent stresses, $\langle \overline{u}_i' \overline{u}_j' \rangle$, computed in LES, are not the true RANS stresses, $\langle u_i' u_j' \rangle$. Here, $\overline{u}_i' = \overline{u}_i - \langle \overline{u}_i \rangle$ denotes the fluctuating velocity field in LES, $u_i' = u_i - \langle u_i \rangle$ denotes the RANS fluctuating velocity field, $\overline{u}_i$ is the velocity field resolved in LES, u_i is the full velocity field and $\langle\ \rangle$ denotes an ensemble average in the spatially homogeneous flow directions and in time. To allow meaningful comparisons between the LES results and the RANS turbulence statistics reported in DNS or experiments, the RANS turbulent stresses were recovered from the turbulent stresses computed in LES using the formulation (Voelkl, Pullin & Chan 2000; Winckelmans *et al.* 2002),

$$\langle u_i' u_j' \rangle \simeq \langle \overline{u}_i' \overline{u}_j' \rangle + \langle \tau_{ij}^* \rangle + \tfrac{2}{3} \delta_{ij} K_{sgs}, \tag{3.5}$$

where $\tau_{ij}^* = \tau_{ij} - \delta_{ij} \tau_{kk}/3$ denotes the deviatoric part of the SGS stress tensor, and $K_{sgs} \equiv \langle \tau_{kk} \rangle / 2$ is the SGS kinetic energy.

Application of (3.5) requires knowledge of K_{sgs}. In LES of incompressible flow, τ_{kk} can be lumped together with the pressure term and solved for implicitly during the course of the simulation. Consequently, most existing SGS models, such as DSM, model only the deviatoric part of the SGS stress tensor and provide no information on τ_{kk}. With such models, the SGS kinetic energy is not directly available from LES, and needs to be recovered at a post-processing stage. In this study, the SGS kinetic energy was recovered from the continuation of the one-dimensional (1-D) energy spectra obtained in LES at each wall-normal location, using an analytical formulation of the 1-D energy spectra in wall flows (Tang & Akhavan 2009; Tang 2015) derived based on Pao's formulation of the three-dimensional (3-D) spectrum for isotropic turbulence (Pao 1965). These analytical 1-D spectra were used to 'continue' the 1-D energy spectra from LES down to the Kolmogorov scale. The SGS kinetic energy was then recovered by integrating the areas under these 'continued' spectra. A similar approach for recovery of the SGS kinetic energy has previously been employed in homogeneous, isotropic turbulence based on analytical or empirical formulations of the 3-D spectra in isotropic turbulence (Knaepen, Debliquy & Carati 2002; Meyers & Baelmans 2004). All the SGS kinetic energies used for the reconstruction of the RANS turbulent intensities, and the Reynolds shear stresses reported in the present study, were obtained from the spectra and velocity fields in the full domain for $z > z^*$, and from the spectra and velocity fields in the minimal flow unit for $z \leqslant z^*$, to take advantage of the additional resolution available in the minimal flow unit for $z \leqslant z^*$.

https://doi.org/10.1017/jfm.2016.137 Published online by Cambridge University Press

$Re_\tau\|_{nom}$	Re_b	$Re_\tau\|_{Dean's}$	$Re_\tau\|_{LES}$	$C_f\|_{Dean's}$	$C_f\|_{LES}$	Error in C_f (%)
1000	20 000	1 016	1 005	5.162×10^{-3}	5.053×10^{-3}	−2.1
2000	45 000	2 066	2 035	4.215×10^{-3}	4.092×10^{-3}	−2.9
5000	125 000	5 051	5 037	3.265×10^{-3}	3.247×10^{-3}	−0.5
10 000	275 000	10 068	10 030	2.681×10^{-3}	2.658×10^{-3}	−0.8
2000^h	45 000	2 066	2 020	4.215×10^{-3}	4.147×10^{-3}	−1.6
5000^h	125 000	5 051	5 009	3.265×10^{-3}	3.230×10^{-3}	−1.1
2000^F	45 000	2 066	1 714	4.215×10^{-3}	2.900×10^{-3}	−31.2
2000^M	45 000	2 066	1 828	4.215×10^{-3}	3.302×10^{-3}	−21.6
$2000^{F,h}$	45 000	2 066	2 030	4.215×10^{-3}	4.071×10^{-3}	−3.4

TABLE 3. The skin friction coefficient, C_f, predicted in nested-LES and non-nested LES of equilibrium turbulent channel flow compared to Dean's correlation (Dean 1978).

4. Results in equilibrium turbulent channel flow

The performance of the nested-LES approach was first assessed in equilibrium turbulent channel flow at $Re_\tau \approx 1000$, 2000, 5000 and 10 000 through comparisons with results from Dean's correlation (Dean 1978), DNS, and experiments.

4.1. *Mean statistics*

Table 3 shows the skin friction coefficients, $C_f \equiv \langle 2\tau_w \rangle / \rho U_b^2$, predicted by nested-LES in equilibrium turbulent channel flow, at standard and high resolutions, compared to Dean's correlation (Dean 1978). The predicted skin friction coefficients were within −2.1 %, −2.9 %, −0.5 % and −0.8 % of values from Dean's correlation at $Re_\tau \approx 1000$, 2000, 5000 and 10 000, respectively, with standard resolution, and within −2 % of the values from Dean's correlation in the high-resolution simulations of 2000^h and 5000^h.

The profiles of the mean velocity, turbulence intensities and Reynolds shear stresses predicted by nested-LES in these flows are shown in figure 3. The mean velocity profiles predicted at $Re_\tau \approx 1000$, 2000 and 5000 show good agreement with available DNS data at $Re_\tau \approx 950$ (del Alamo *et al.* 2004), $Re_\tau \approx 2000$ (Hoyas & Jimenez 2006), $Re_\tau \approx 5200$ (Lee & Moser 2015) and experimental data at $Re_\tau \approx 4800$ (Comte-Bellot 1963), respectively. At $Re_\tau \approx 10\,000$, no DNS data is currently available. Consequently, the nested-LES results were assessed based on a combination of DNS data at $Re_\tau \approx 5200$ (Lee & Moser 2015) and experimental data at $Re_\tau \approx 8600$ (Comte-Bellot 1963). The original experimental data at $Re_\tau \approx 8600$ published by Comte-Bellot (1963) displays a mean velocity profile which is shifted relative to the universal law of the wall. In the present study, this experimental data is displayed after adjusting the value of the wall friction velocity, u_τ, in the experiments to bring the experimental data into agreement with the universal law of the wall. All the experimental data of Comte-Bellot (1963) at $Re_\tau \approx 8600$ shown in the present study have been normalized using this adjusted u_τ.

The mean velocity profiles predicted by nested-LES exhibit the correct behaviour throughout the cross-section of the channel at all Reynolds numbers, including the correct slope in the logarithmic layer, and agreement with DNS and experimental data in the wake region. Furthermore, no change in slope or other anomalies are observed in the mean velocity profiles at $z = z^*$. The high-resolution cases of 2000^h and 5000^h predict mean velocity profiles which are virtually indistinguishable from

https://doi.org/10.1017/jfm.2016.137 Published online by Cambridge University Press

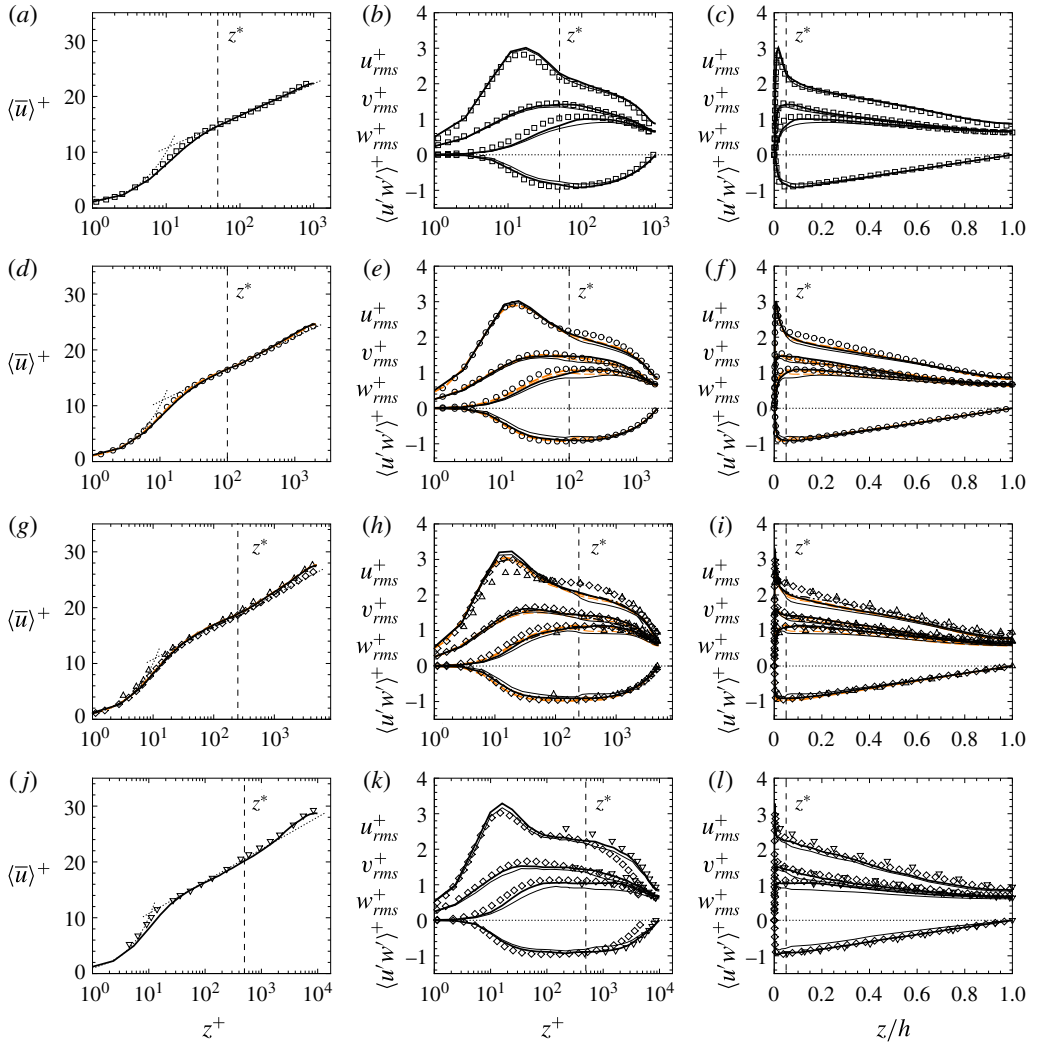


FIGURE 3. Profiles of the mean velocity, turbulence intensities and Reynolds shear stress predicted by nested-LES in equilibrium turbulent channel flow at (*a–c*) $Re_\tau \approx 1000$, (*d–f*) $Re_\tau \approx 2000$, (*g–i*) $Re_\tau \approx 5000$, (*j–l*) $Re_\tau \approx 10\,000$, compared to DNS and experimental data. ——, nested-LES performed at standard resolution; – – –, (orange), nested-LES cases of 2000^h and 5000^h, performed at high resolution; thick lines, mean velocity, RANS turbulence intensities, $\langle u'_\alpha u'_\alpha\rangle^{1/2}$, and Reynolds shear stress, $\langle u'w'\rangle$, reconstructed from nested-LES results using (3.5); thin lines, turbulence intensities, $\langle \overline{u}'_\alpha \overline{u}'_\alpha\rangle^{1/2}$, and Reynolds shear stress, $\langle \overline{u}'\overline{w}'\rangle$, predicted by nested-LES without reconstruction; □, DNS at $Re_\tau \approx 950$ (del Alamo *et al.* 2004); ○, DNS at $Re_\tau \approx 2000$ (Hoyas & Jimenez 2006); ◇, DNS at $Re_\tau \approx 5200$ (Lee & Moser 2015); △, experiments at $Re_\tau \approx 4800$ (Comte-Bellot 1963); ▽, experiments at $Re_\tau \approx 8600$ (Comte-Bellot 1963); – · · –, LES at $Re_\tau \approx 4000$ (Kravchenko, Moin & Moser 1996); · · · · · ·, the asymptotes $\langle\overline{u}\rangle^+ = z^+$, and $\langle\overline{u}\rangle^+ = 2.5\ln(z^+) + 5$.

those obtained at standard resolution, consistent with the close agreement between the C_f values of the standard- and high-resolution cases.

Good agreement is also observed in figure 3 between the turbulence intensities and Reynolds shear stresses predicted by nested-LES and available DNS and experimental

https://doi.org/10.1017/jfm.2016.137 Published online by Cambridge University Press

data. To allow direct comparison of the nested-LES predictions with available DNS and experimental data, the true RANS turbulence intensities, $\langle u'_\alpha u'_\alpha \rangle^{1/2}$, were reconstructed from the LES results using (3.5) and shown in figure 3. For reference, the LES turbulence intensities, $\langle \overline{u}'_\alpha \overline{u}'_\alpha \rangle^{1/2}$, without reconstruction are also shown. Unlike most existing wall modelling approaches, which only provide the turbulence statistics in the outer layer, the nested-LES approach can provide accurate predictions of the turbulent statistics in both the inner and outer layers. Both the locations and magnitudes of the near-wall peaks of the turbulence intensities are accurately predicted at all Reynolds numbers, with the magnitude of the near-wall peak of the streamwise turbulence intensity showing a gradual increase with increasing Reynolds number, consistent with recent observations in experiments (Marusic *et al.* 2010*b*) and DNS (Hoyas & Jimenez 2006; Schlatter *et al.* 2010). The overprediction of the near-wall peak of the streamwise turbulence intensity by 3–7 % at standard resolution, and by less than 1 % at high resolution, and underprediction of the streamwise turbulence intensities in the logarithmic layer by up to 10–15 % at both resolutions, observed in figure 3 compared to DNS, are both features of DSM which have also been observed in a number of prior studies. An example of such studies, performed with DSM using well-resolved conventional LES at $Re_\tau \approx 4000$ (Kravchenko *et al.* 1996; Cabot & Moin 1999), is also shown in figure 3(*g–i*). Similar differences of up to 5 %, 10 % and 5 % at standard resolution, and up to 3 %, 6 % and 2 % at high resolution, are also observed in figure 3 in the prediction of the spanwise and wall-normal turbulent intensities and the Reynolds shear stress, respectively, compared to DNS.

The high-resolution cases of 2000^h and 5000^h predict reconstructed RANS turbulence intensities and a Reynolds shear stress within 5 % of the results from the standard resolution for $z^+ \leqslant 200$, and within 2 % of the results from the standard resolution in the rest of the channel, indicating the invariance of the results to the resolution of the grid.

Recovery of the SGS stresses leads to differences of up to 5 %, 12 % and 16 %, at standard resolution, and up to 3 %, 8 % and 12 % at high resolution, between the RANS and LES turbulence intensities in the streamwise, spanwise and wall-normal directions, respectively.

4.2. *Energy spectra*

Figure 4 shows the 1-D energy spectra of the components of the fluctuating velocity predicted by nested-LES in turbulent channel flow at $1000 \leqslant Re_\tau \leqslant 10\,000$ in the outer layer ($z/h \approx 0.5$) and near-wall region ($z^+ \approx 20$), compared to DNS data of Hoyas & Jimenez (2006) at $Re_\tau \approx 2000$. The nested-LES spectra are normalized using the kinematic viscosity, ν, and plane-averaged rates of TKE dissipation, defined as $\langle \epsilon \rangle \equiv \langle 2\nu \overline{s}'_{ij} \overline{s}'_{ij} + \overline{s}'_{ij} \tau_{ij} \rangle$, where $\overline{s}'_{ij} = (\partial \overline{u}'_i / \partial x_j + \partial \overline{u}'_j / \partial x_i)/2$ is the resolved fluctuating strain rate tensor, τ_{ij} is the modelled SGS stress tensor and $\langle\ \rangle$ denotes ensemble averaging in space, over the homogeneous flow directions, and in time.

In the outer layer ($z/h \approx 0.5$), the full-domain spectra span the range of scales from the largest eddies in the computational domain down to inertial-range eddies, while the minimal-flow-unit spectra span the range of scales from inertial-range eddies down to dissipation-range eddies. The full-domain spectra display a region conforming to $\sim k^{-5/3}$ asymptote in the inertial range, and a Reynolds number dependent peel-off from the $k^{-5/3}$ asymptote in the energy-containing scales, as anticipated. The largest scales of the minimal flow unit, which fall in the inertial range, also have a $\sim k^{-5/3}$ asymptote, but are shifted relative to the inertial range of the full domain because

https://doi.org/10.1017/jfm.2016.137 Published online by Cambridge University Press

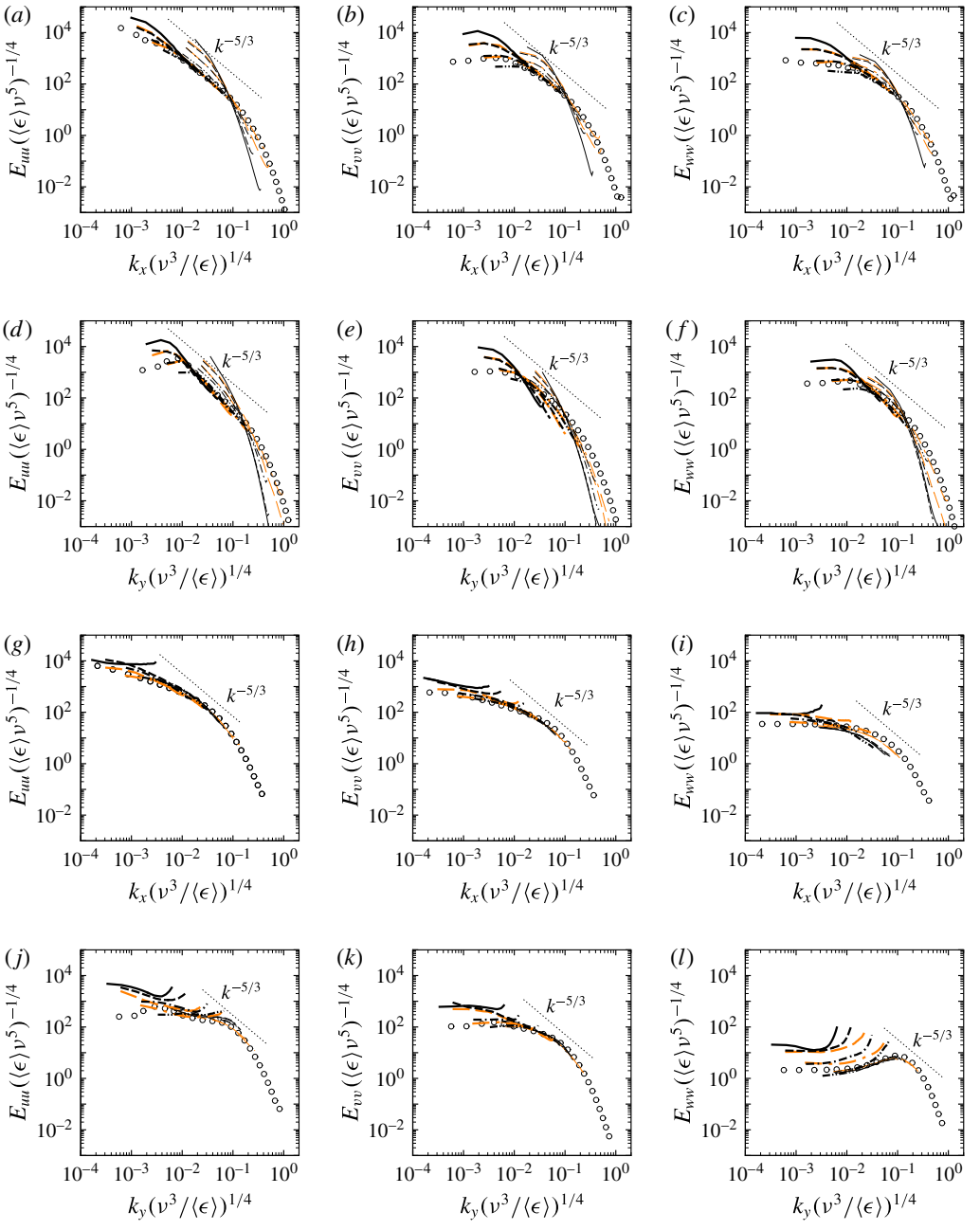


FIGURE 4. One-dimensional energy spectra of the streamwise, spanwise, and wall-normal velocity fluctuations, predicted by nested-LES in equilibrium turbulent channel flow at $1000 \leqslant Re_\tau \leqslant 10\,000$ in (*a–f*) outer region ($z/h \approx 0.5$), (*g–l*) near-wall region ($z^+ \approx 20$): (*a–c*,*g–i*), energy spectra in the streamwise direction; (*d–f*,*j–l*), energy spectra in the spanwise direction. – · · –, $Re_\tau \approx 1000$; – · –, $Re_\tau \approx 2000$; – – –, $Re_\tau \approx 5000$; ——, $Re_\tau \approx 10\,000$; — · — (orange), $Re_\tau \approx 2000^h$ high resolution; — — (orange), $Re_\tau \approx 5000^h$ high resolution; thick lines, spectra in the full domain of nested-LES; thin lines, spectra in the minimal flow unit of nested-LES; ○, DNS at $Re_\tau \approx 2000$ (Hoyas & Jimenez 2006).

https://doi.org/10.1017/jfm.2016.137 Published online by Cambridge University Press

these scales need to absorb the energy in the energy-containing scales of the full domain which are absent in the minimal flow unit. At the small scales, the minimal-flow-unit spectra display a drop-off in the dissipation range which is sharper than that in DNS due to the presence of SGS dissipation in nested-LES. With decreasing Reynolds number or increasing resolution, as in high resolution cases of 2000^h and 5000^h, the dissipation-range spectra begin to approach those in DNS. In the energy-containing and inertial-range scales, the predicted spectra for cases 5000 and 5000^h show good agreement with each other, while those for cases 2000 and 2000^h show good agreement with each other and with DNS data (Hoyas & Jimenez 2006).

In the near-wall region ($z^+ \approx 20$), the spectra in the minimal flow unit at different Reynolds numbers and different resolutions all collapse and agree with DNS, reflecting the presence of sufficient resolution in the minimal flow unit of nested-LES in the near-wall region. The full-domain spectra in the near-wall region capture the large-scale features observed in the DNS spectra, and show an upshift of the spectra in the largest scales with increasing Reynolds number.

4.3. *High-order moments*

Recent experiments in high Reynolds number turbulent boundary layers and pipe flows (Hultmark *et al.* 2013; Marusic *et al.* 2013; Meneveau & Marusic 2013) have confirmed that the variance of the streamwise velocity fluctuations exhibits logarithmic behaviour within an inertial sublayer, consistent with, and supportive of, earlier predictions by models based on the 'attached-eddy' hypothesis (Townsend 1976; Perry, Henbest & Chong 1986). It has further been shown (Meneveau & Marusic 2013) that this logarithmic behaviour can be generalized to all even-order moments of the streamwise velocity fluctuations as,

$$\langle (u'^+)^{2p} \rangle^{1/p} = -A_p \ln (z/\delta) + B_p = -A_p \ln (z^+) + D_p(Re_\tau), \tag{4.1}$$

where the coefficients A_p are the generalized 'Townsend–Perry' constants for moments of order $2p$, and appear quite insensitive to the Reynolds number, while B_p and D_p are non-universal constants.

It has been suggested that the ability of LES to reproduce this logarithmic behaviour in the higher-order moments of the streamwise velocity fluctuations, with generalized 'Townsend–Perry' constants, A_p, in agreement with experiments, should be used as an additional criterion for evaluation of the capability of LES to capture the fundamental scaling laws and inherent nonlinear dynamics of turbulence (Stevens, Wilczek & Meneveau 2014). Furthermore, it has been reported that for wall-modelled conventional LES to faithfully reproduce these generalized 'Townsend–Perry' constants, a fine resolution is required in the simulations (Stevens *et al.* 2014).

In this section, we explore the ability of the nested-LES approach to predict this logarithmic behaviour in the even-order moments of the streamwise velocity fluctuations. Figure 5(*a*,*b*) show the second ($2p = 2$) and sixth ($2p = 6$) order moments of the streamwise velocity fluctuations, $\langle (u'^+)^{2p} \rangle^{1/p}$, predicted by nested-LES at $1000 \leqslant Re_\tau \leqslant 10\,000$, respectively, while figure 5(*c*) shows the even-order moments for $2 \leqslant 2p \leqslant 12$ at $Re_\tau = 10\,000$. A logarithmic behaviour can be observed in all the even-order moments displayed in figure 5(*a–c*) over the range $z^+ > 3Re^{1/2}$ and $z/h < 0.30$, for which the logarithmic behaviour has been observed in experiments (Marusic *et al.* 2013; Meneveau & Marusic 2013). The data shown in figure 5(*c*) indicates that the logarithmic behaviour may extend beyond $z/h \sim 0.3$ with increasing

https://doi.org/10.1017/jfm.2016.137 Published online by Cambridge University Press

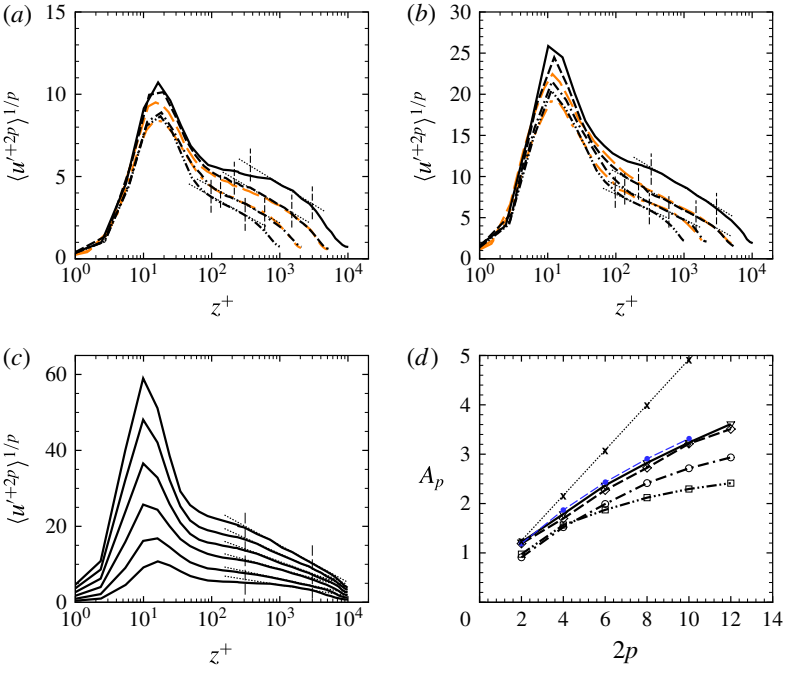


FIGURE 5. Moments of order (*a*) $2p=2$, (*b*) $2p=6$, (*c*) $2p=2$, 4, 6, 8, 10, 12 (raised to the power of $1/p$) of the streamwise velocity fluctuations, (*d*) coefficients, A_p, in the logarithmic law for moments, as a function of the moment order, $2p$, predicted by nested-LES at $1000 \leqslant Re_\tau \leqslant 10\,000$. – ·· –, $Re_\tau \approx 1000$; – · –, $Re_\tau \approx 2000$; – – –, $Re_\tau \approx 5000$; ——, $Re_\tau \approx 10\,000$; — · — (orange), $Re_\tau \approx 2000^h$ high-resolution; — — (orange), $Re_\tau \approx 5000^h$ high-resolution; –●– (blue), experiments in TBL at $Re_\tau \approx 19030$ (Meneveau & Marusic 2013); ···×···, Gaussian values for $A_p = A_1[(2p-1)!!]^{1/p}$ with $A_1 = 1.25$; ·····, logarithmic fit to the region $3Re_\tau^{1/2} \leqslant z^+ \leqslant 0.3Re_\tau$; the dashed vertical lines in (*a–c*) denote the bounds of the region $3Re_\tau^{1/2} \leqslant z^+ \leqslant 0.3Re_\tau$.

order of the moments. Nevertheless, the coefficients A_p and D_p in (4.1) were obtained by a least squares fit to the moments between $z^+ > 3Re^{1/2}$ and $z/h < 0.30$.

Figure 5(*d*) shows the values of the coefficients A_p, for $2 \leqslant 2p \leqslant 12$, obtained from nested-LES results at $1000 \leqslant Re_\tau \leqslant 10\,000$. For reference, the A_p coefficients from experimental measurements in TBL at $Re_\tau \approx 19\,030$ (Meneveau & Marusic 2013) are also shown. The A_p coefficients obtained from nested-LES at $Re_\tau \approx 10\,000$ show good agreement with the A_p coefficients from TBL experiments at $Re_\tau \approx 19\,030$, indicating the insensitivity of the A_p coefficients to the Reynolds number at high enough Reynolds numbers. At low Reynolds numbers ($Re_\tau \leqslant 2000$), the trends in A_p coefficients from nested-LES are similar to those observed at low Reynolds numbers in experiments (Meneveau & Marusic 2013). At all Reynolds numbers, the A_p coefficients from both nested-LES and experiments show sub-Gaussian behaviour. The limiting asymptotic behaviour of the A_p coefficient at high Reynolds numbers indicates that this sub-Gaussian scaling of the moments does not become more Gaussian with increasing Reynolds number.

Further evidence of the sub-Gaussian behaviour of the streamwise velocity fluctuations is observed in the plots of skewness and flatness, as shown in figure 6. Both the skewness and flatness of the streamwise velocity fluctuations display

https://doi.org/10.1017/jfm.2016.137 Published online by Cambridge University Press

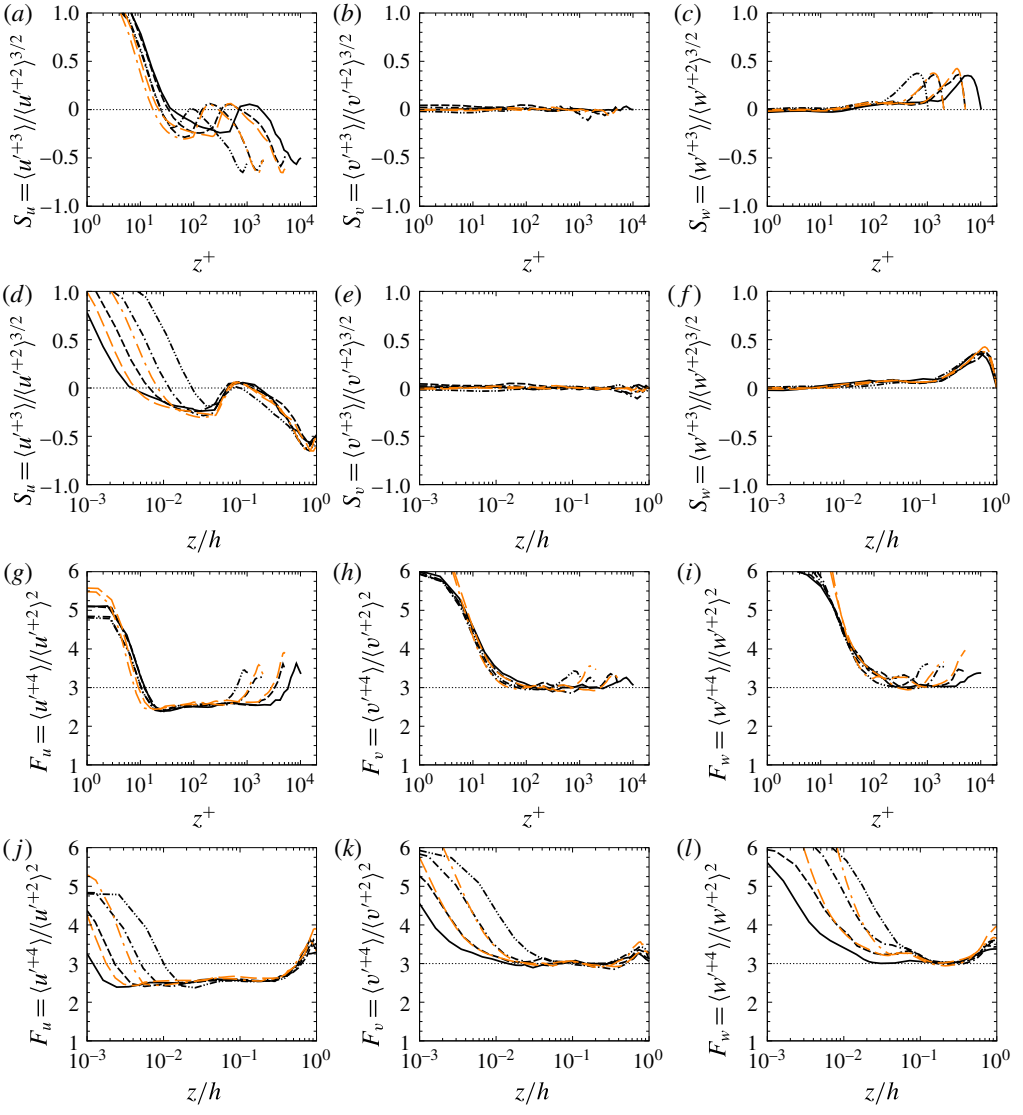


FIGURE 6. Skewness (*a–f*), and flatness (*g–l*) of the streamwise (*a*,*d*,*g*,*j*), spanwise (*b*,*e*,*h*,*k*) and wall-normal (*c*,*f*,*i*,*l*) velocity fluctuations as a function of z^+ (*a–c*,*g–i*), and z/h (*d–f*,*j–l*). Line types as in figure 4.

sub-Gaussian behaviour in the logarithmic region. A sign change is observed in the skewness of the streamwise velocity fluctuations in the inner layer ($z/h < 0.1$). A similar sign change in the sign of S_u has been reported experimentally, but only in the buffer layer and of much weaker negative magnitude (Marusic, Mathis & Hutchins 2010*a*). The profiles of the flatness of the streamwise velocity fluctuations show similar trends to experiments in TBL (Meneveau & Marusic 2013). The spanwise velocity fluctuations display near-Gaussian behaviour throughout the logarithmic layer, with skewness and flatness values near the Gaussian values of 0 and 3, respectively. The wall-normal velocity fluctuations display slightly super-Gaussian behaviour with a slightly positive skewness and flatness values slightly higher than the Gaussian values.

https://doi.org/10.1017/jfm.2016.137 Published online by Cambridge University Press

4.4. *Two-point statistics*

The previous sections have established the ability of nested-LES to faithfully predict the one-point statistics and spectra in turbulent channel flow. In this section, we investigate the ability of nested-LES to predict structural features of the flow. To this end, we examine the two-point correlations obtained from nested-LES in turbulent channel flow.

The two-point correlation coefficient, $C_{\varphi\varphi}$, is defined as

$$C_{\varphi\varphi}(\boldsymbol{r}, \boldsymbol{r}') = \frac{\langle \varphi(\boldsymbol{r})\varphi(\boldsymbol{r}')\rangle}{\sigma_\varphi(\boldsymbol{r})\sigma_\varphi(\boldsymbol{r}')}, \tag{4.2}$$

where φ denotes the streamwise, spanwise or wall-normal velocity fluctuations, $\boldsymbol{r} = (x, y, z)$ and $\boldsymbol{r}' = (x', y', z')$ are the coordinates of the reference point and the moving point, respectively, $\langle\ \rangle$ denotes ensemble averaging in time and in homogeneous directions, and $\sigma_\varphi(\boldsymbol{r})$ and $\sigma_\varphi(\boldsymbol{r}')$ are the standard deviations of φ evaluated at $\boldsymbol{r}$ and $\boldsymbol{r}'$, respectively.

Figure 7 shows the streamwise (x–z plane) and spanwise (y–z plane) sections of the contour maps of C_{uu}, C_{vv}, C_{ww} at $z/h = 0.1$ and $z/h = 0.6$, based on data from nested-LES at $1000 \leqslant Re_\tau \leqslant 10\,000$. The contour maps of the correlation coefficients at different Reynolds numbers show a reasonable collapse, with the exception of the weakly correlated structures of C_{uu}. This lack of a simple Reynolds number scaling for the C_{uu} structures has been reported in several prior studies (del Alamo *et al.* 2004; Jimenez & Hoyas 2008; Sillero, Jimenez & Moser 2014). The weakly correlated contours of C_{uu} (contours of $C_{uu} \leqslant 0.1$) suggest a size of structures of the order of $O(4h)$, which is much smaller than the $O(18h)$ reported by Sillero *et al.* (2014) in DNS of turbulent channel flow at $Re_\tau \approx 950$, due to the smaller domain size employed in the present studies. Other features of the structures are consistent with those reported by Sillero *et al.* (2014). On the streamwise section, the streamwise and spanwise velocity fluctuations both exhibit structures which are inclined to the wall. The structures of C_{vv} are inclined at a steeper angle than those of C_{uu}, and exhibit structures with negative correlation above and underneath the ones with positive correlation, indicating the presence of inclined mean vortical motions, consistent with those observed in many earlier studies (Robinson 1991). On the spanwise section, the structures of C_{uu} exhibit a pattern of alternating high- and low-velocity regions, while the structures of C_{vv} display negative contours below and above the positive core, and those of C_{ww} show negative contours on the sides of the positive core, both indicating evidence of quasi-streamwise vortical structures.

From the contours in the streamwise section, we have computed the inclination angles, $\theta_{\varphi\varphi}$, of the structures by fitting a line through the two points which are furthest away upstream and downstream from the reference location at each contour level between 0.2 and 0.7 (Wu & Christensen 2010). The values of $\theta_{\varphi\varphi}$ obtained at all contour levels and for all Reynolds numbers are then averaged at each wall-normal location. Samples of the resulting values for θ_{uu} and θ_{vv} are shown in figure 7(*a*,*c*,*g*,*i*).

Figure 8 shows the variation of the inclination angles, θ_{uu}, θ_{vv} and θ_{ww}, as a function of the distance from the wall, from the nested-LES results at $1000 \leqslant Re_\tau \leqslant 10\,000$, compared to the inclination angles reported from DNS of turbulent channel flow at $Re_\tau \approx 950$ (del Alamo *et al.* 2004; Sillero *et al.* 2014). In the channel core, the inclination angles predicted by nested-LES asymptote to values of 10°, 25° and 90° for θ_{uu}, θ_{vv}, and θ_{ww}, respectively, which agree reasonably well with the inclination angles reported by Sillero *et al.* (2014) in DNS of turbulent channel flow at $Re_\tau \approx 950$.

https://doi.org/10.1017/jfm.2016.137 Published online by Cambridge University Press

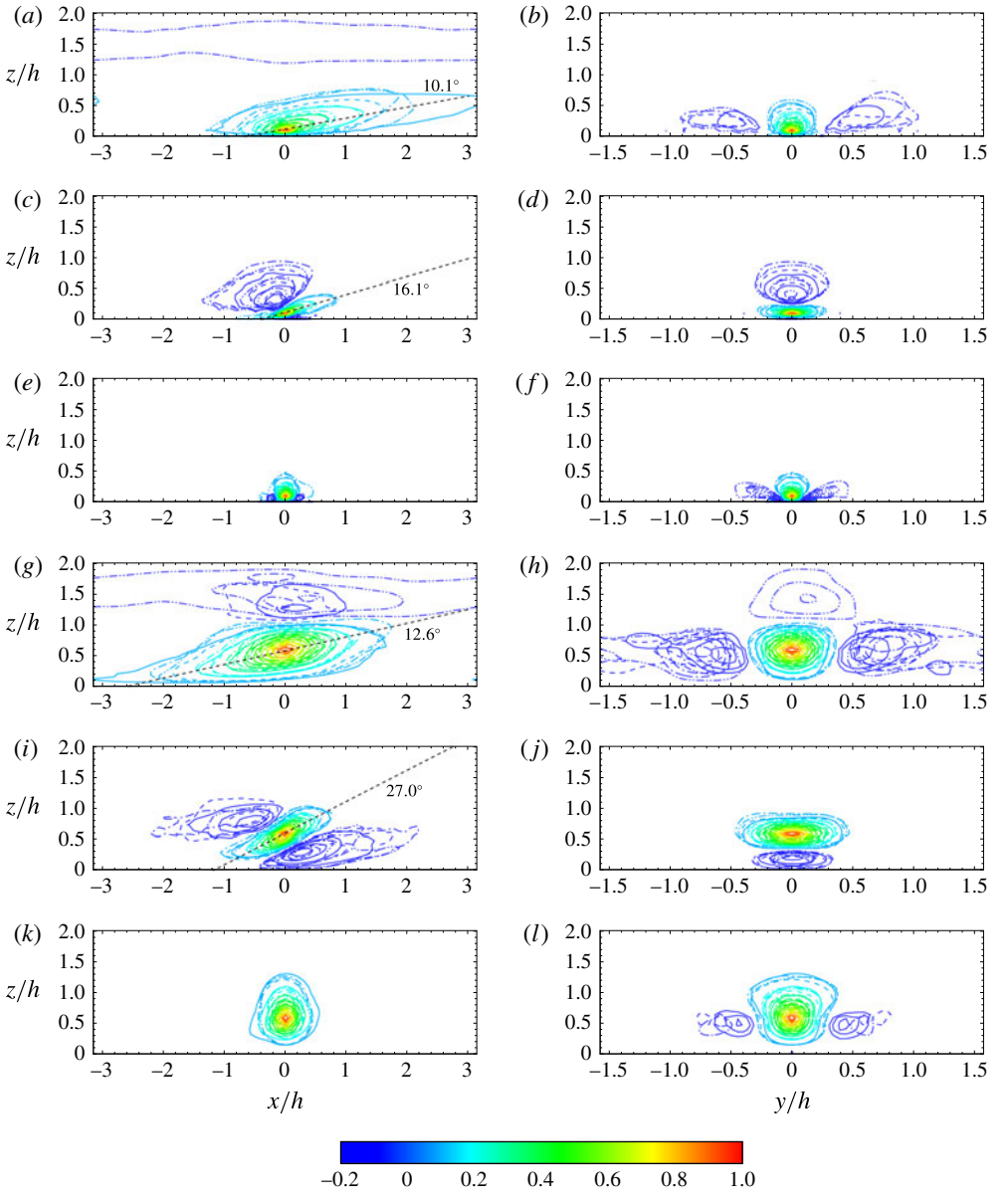


FIGURE 7. Streamwise (xz) (a,c,e,g,i,k), and spanwise (yz) (b,d,f,h,j,l) sections of the correlation maps predicted by nested-LES in equilibrium turbulent channel flow at $1000 \leqslant Re_\tau \leqslant 10\,000$ at (a–f) $z/h = 0.1$, and (g–l) $z/h = 0.6$: (a,b,g,h) C_{uu}; (c,d,i,j) C_{vv}; (e,f,k,l) C_{ww}. – · · –, $Re_\tau \approx 1000$; – · –, $Re_\tau \approx 2000$; – – –, $Re_\tau \approx 5000$; ——, $Re_\tau \approx 10\,000$. Positive contours are shown at $(0.1 : 0.1 : 0.9)$; negative contours are shown at $(-0.05 : -0.05 : -0.20)$, where available, except in (f,l), where negative contours are shown at $(-0.01 : -0.02 : -0.09)$, where available.

The discrepancies observed in figure 8 can be attributed to the different methodologies used for obtaining the inclination angles in the present study compared to Sillero *et al.* (2014).

https://doi.org/10.1017/jfm.2016.137 Published online by Cambridge University Press

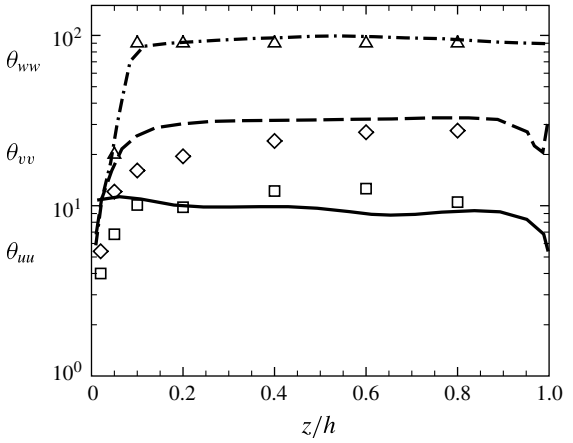


FIGURE 8. Inclination angles predicted by nested-LES in equilibrium turbulent channel flow at $1000 \leqslant Re_\tau \leqslant 10\,000$, compared to DNS results at $Re_\tau \approx 950$ (del Alamo *et al.* 2004; Sillero *et al.* 2014). □, ◇, △, inclination angles θ_{uu}, θ_{vv}, θ_{ww}, respectively, predicted by nested-LES; ——, – – –, – · –, inclination angles, θ_{uu}, θ_{vv}, θ_{ww}, respectively, predicted by DNS.

Figure 9 shows the 1-D two-point correlation functions predicted by nested-LES for all components of the velocity fluctuations in the outer layer ($z/h \approx 0.5$) and the near-wall region ($z^+ \approx 10$). The 1-D two-point correlations at $z^+ \approx 10$ were computed from the minimal flow unit of nested-LES, and show evidence of the presence of a streaky structure with a streak spacing of $\sim$100 wall units in the near-wall region in (figure 9*e*). This indicates that the near-wall dynamics is adequately captured by nested-LES. As with all LES, the diameter of the near-wall streamwise vortices is overpredicted by nested-LES in (figure 9*e*), because the grid spacing of $\Delta_y^+ \approx 25$–30, employed in the minimal flow unit of nested-LES, is of the same order as the diameter of these structures.

From the two-point correlation functions, one may obtain a measure of the average size of the structures by computing the integral length scales, $\Lambda_{\alpha,\varphi}$, given by

$$\Lambda_{\alpha,\varphi} = \int C_{\varphi\varphi}(\boldsymbol{r}, \boldsymbol{r}')\, \mathrm{d}r_\alpha, \tag{4.3}$$

where r_α denotes x, y or z. The integrals in (4.3) were computed only to $C_{\varphi\varphi} = 0.05$, to avoid the noisy correlation tails and long negative regions in $C_{\varphi\varphi}$, which could cancel out the positively correlated regions (Sillero *et al.* 2014).

Figure 10 shows the integral length scales as a function of the wall-normal distance, from nested-LES at $1000 \leqslant Re_\tau \leqslant 10\,000$. The sizes of the structures, as inferred from $\Lambda_{\alpha,\varphi}(z)$, better motivate the construction of the grid and the choice of $z^*/h = 0.05$ in the present study. From figure 10, it can be seen that for $z \geqslant z^*$, the structures have a size $\Lambda_{x,\varphi} > 0.15$, $\Lambda_{y,\varphi} > 0.07$ and $\Lambda_{z,\varphi} > 0.07$. Therefore, for $z > z^*$, the grid spacings of $\Delta_x/h = 0.1$, $\Delta_y/h = 0.05$ and $\Delta_z/h \approx 0.05$, employed in the full domain of nested-LES in the present study, can adequately resolve these structures. However, for $z < z^*$, $\Lambda_{x,v}/h$ and $\Lambda_{x,w}/h$ become comparable to Δ_x/h, while $\Lambda_{y,w}/h$ becomes smaller than Δ_y/h in the full domain. Thus the full domain can no longer properly resolve these structures, and the basis for renormalization of the velocity field in (2.2)–(2.4) needs to be switched from the full domain to the minimal flow unit.

https://doi.org/10.1017/jfm.2016.137 Published online by Cambridge University Press

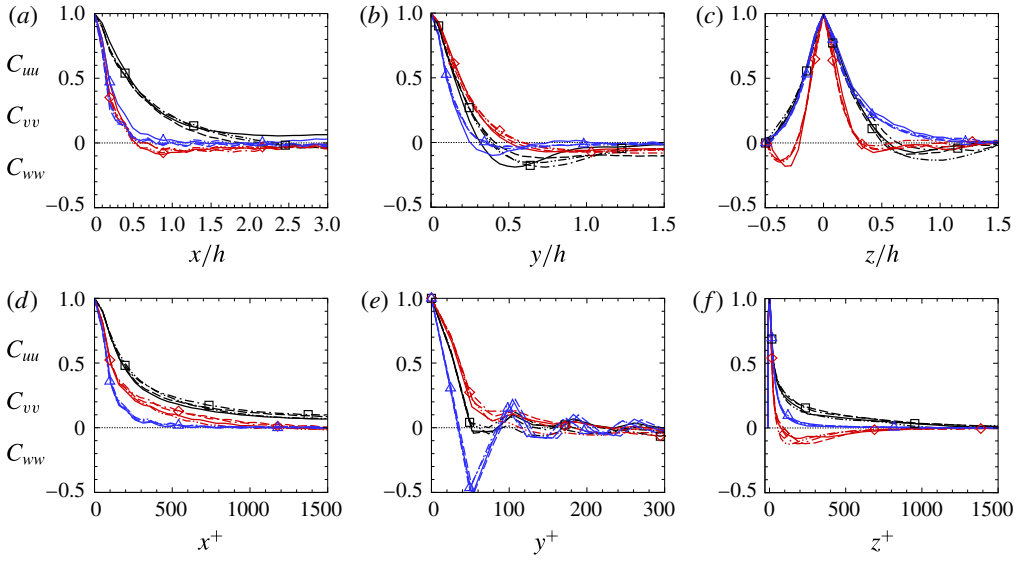


FIGURE 9. Two-point correlations predicted by nested-LES in equilibrium turbulent channel flow at $1000 \leqslant Re_\tau \leqslant 10\,000$ in (*a–c*) the outer region ($z/h \approx 0.5$), obtained from the full domain; (*d–f*) the near-wall region ($z^+ \approx 10$), obtained from the minimal flow unit. Black lines with □, C_{uu}; red lines with ◇, C_{vv}; blue lines with △, C_{ww}; line types as in figure 4.

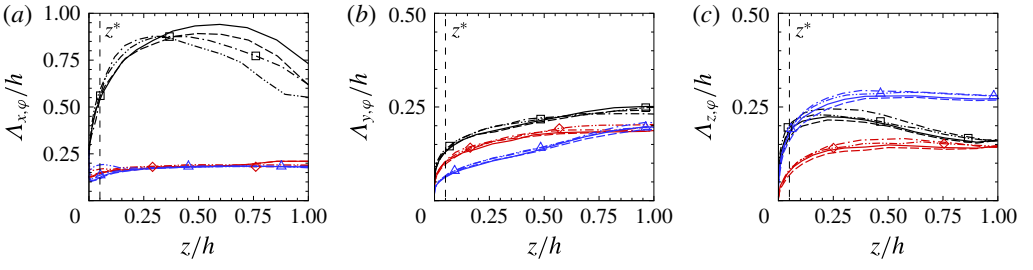


FIGURE 10. The integral scales, $\Lambda_{\alpha,\varphi}$, predicted by nested-LES in equilibrium turbulent channel flow at $1000 \leqslant Re_\tau \leqslant 10\,000$. Black lines with □, $\Lambda_{\alpha,u}$; red lines with ◇, $\Lambda_{\alpha,v}$; blue lines with △, $\Lambda_{\alpha,w}$; line types as in figure 4.

The $\Lambda_{z,\varphi}$ of figure 10 also motivate the construction of the grid and the required number of grid points in the wall-normal direction. In the wake region ($z/h > 0.1$), the $\Lambda_{z,\varphi}$ nearly plateau and all $\Lambda_{z,\varphi}/h$ have values greater than 0.1. Consequently a fixed number of grid points with a nearly uniform grid of size $\Delta_z/h \approx 0.05$–0.1 can properly resolve the turbulence structures in this region at all Reynolds numbers. In contrast, for $z/h < 0.1$, the size of $\Lambda_{z,\varphi}$ grows approximately linearly with the distance from the wall, and $O(\log Re_\tau)$ grid points are needed to resolve these structures, as shown in § 6.

4.5. *Effect of z^**

We next examine the effect of placement of z^*, the wall-normal location at which the basis for renormalization of the velocity field is switched from the velocity field in

https://doi.org/10.1017/jfm.2016.137 Published online by Cambridge University Press

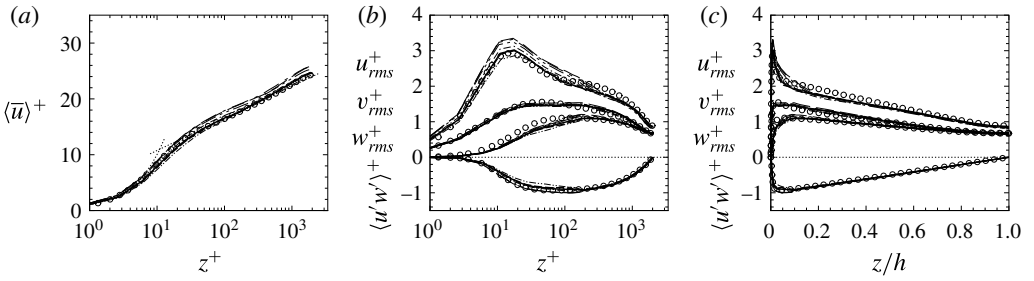


FIGURE 11. Effect of z^*/h on the profiles of the mean velocity, turbulence intensities, and Reynolds shear stress predicted by nested-LES in equilibrium turbulent channel flow at $Re_\tau \approx 2000$. – · · –, $z^*/h = 0.025$; – – –, $z^*/h = 0.04$; ——, $z^*/h = 0.05$; – · –, $z^*/h = 0.07$; — · ·—, $z^*/h = 0.10$; — · —, $z^*/h = 0.15$; — —, $z^*/h = 0.20$; ○, DNS at $Re_\tau \approx 2000$ (Hoyas & Jimenez 2006).

$Re_\tau\|_{nom}$	z^*/h	$C_f\|_{Dean's}$	$C_f\|_{LES}$	Error in C_f (%)
2000	0.025	4.215×10^{-3}	4.254×10^{-3}	+0.9
2000	0.040	4.215×10^{-3}	4.141×10^{-3}	−1.8
2000	0.050	4.215×10^{-3}	4.092×10^{-3}	−2.9
2000	0.070	4.215×10^{-3}	4.053×10^{-3}	−3.8
2000	0.100	4.215×10^{-3}	3.883×10^{-3}	−7.9
2000	0.150	4.215×10^{-3}	3.728×10^{-3}	−11.5
2000	0.200	4.215×10^{-3}	3.786×10^{-3}	−10.2

TABLE 4. The skin friction coefficient, C_f, predicted in nested-LES of equilibrium turbulent channel flow at $Re_\tau \approx 2000$ with different locations of z^*/h.

the minimal flow unit (for $z \leqslant z^*$) to the velocity field in the full domain (for $z > z^*$), on the predicted flow statistics and structure. To this end, nested-LES were performed at $Re_\tau \approx 2000$ with $z^*/h = 0.025$, 0.04, 0.07, 0.10, 0.15 and 0.20.

The results are summarized in table 4 and figure 11. The most accurate predictions of C_f and the mean statistics are obtained with $z^*/h = 0.04$ or 0.05. When z^*/h is moved closer to the wall, the computations become under-resolved between $z^*/h < z/h < 0.05$ because of the coarse grid spacings in the x and y directions in the full domain. When z^*/h is moved above $z/h = 0.05$, the computations suffer from the inadequate size of the minimal flow unit in the region $0.05 < z/h < z^*/h$. It appears that the best results are obtained when the solution is switch from the minimal flow unit to the full domain as soon as the grid resolution in the full domain becomes adequate.

While choosing a non-optimal value of z^* slightly degrades the performance of nested-LES, it is not catastrophic. The effect is even less prominent in the prediction of the flow structures, as shown in figure 12, where the streamwise and spanwise sections of two-point correlation coefficient, $C_{\varphi\varphi}$, for all components of the velocity fluctuations at $z/h = 0.1$ and $z/h = 0.6$, are plotted for nested-LES at $Re_\tau \approx 2000$ with $z^*/h = 0.025$, 0.04, 0.04 and 0.07. The contours of $C_{\varphi\varphi}$ predicted with different z^* are seen to nearly collapse, with the exception of the large, weakly correlated structures for C_{uu}.

https://doi.org/10.1017/jfm.2016.137 Published online by Cambridge University Press

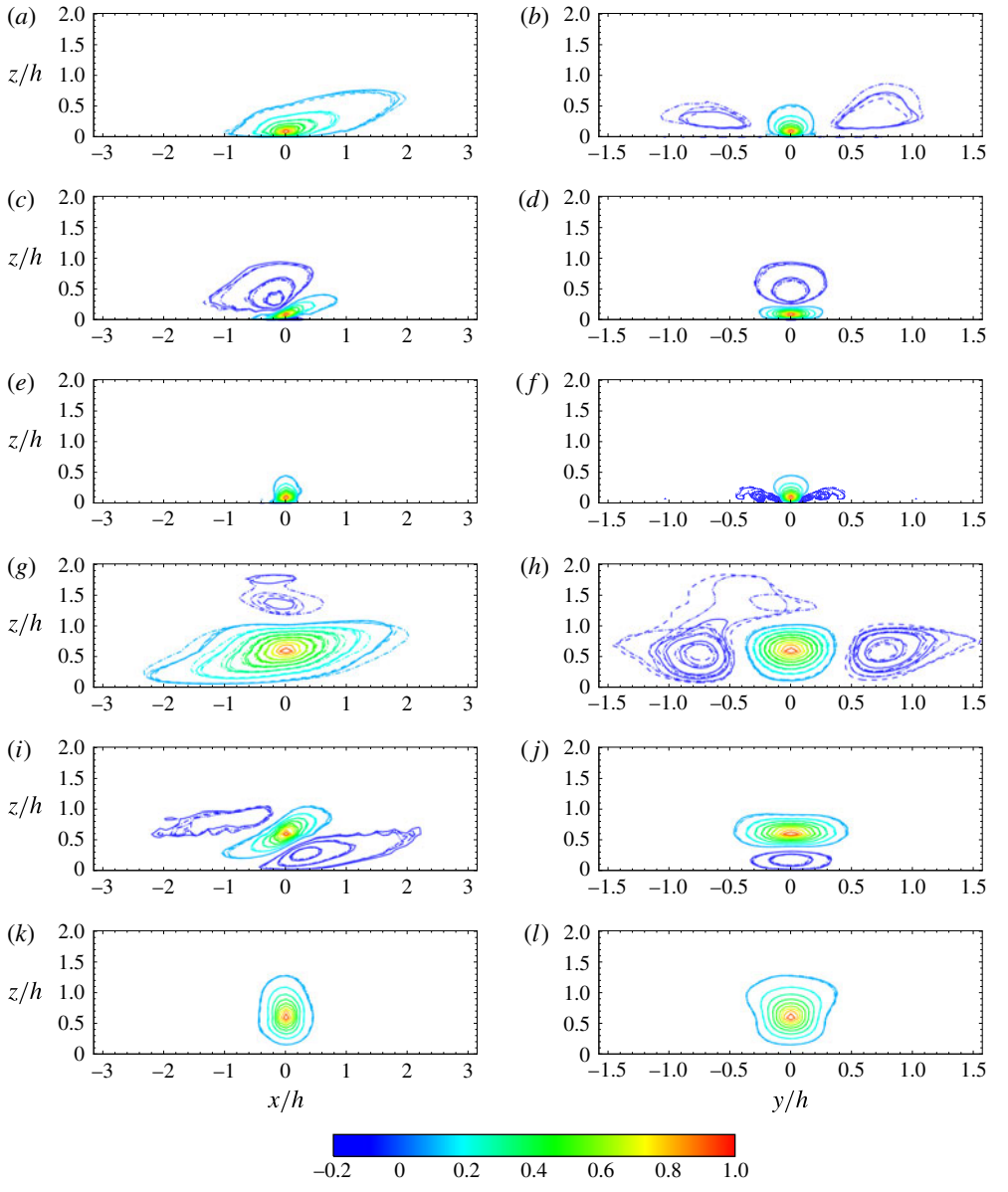


FIGURE 12. Streamwise (xz) (a,c,e,g,i,k), and spanwise (yz) (b,d,f,h,j,l) sections of the correlation maps predicted by nested-LES in equilibrium turbulent channel flow at $Re_\tau \approx 2000$ with z^* placed at $z^*/h = 0.025$, 0.04, 0.05, and 0.07: (a–f) $z/h = 0.1$, (g–l) $z/h = 0.6$; (a,b,g,h) C_{uu}; (c,d,i,j) C_{vv}; (e,f,k,l) C_{ww}. Line types as in figure 11; contour levels as in figure 7.

4.6. *Renormalization functions*

The ability of nested-LES to accurately predict the turbulence statistics, structures and spectra results from only minor renormalizations of the velocity fields in the full domain and minimal flow unit at each time step during the course of the simulation.

https://doi.org/10.1017/jfm.2016.137 Published online by Cambridge University Press

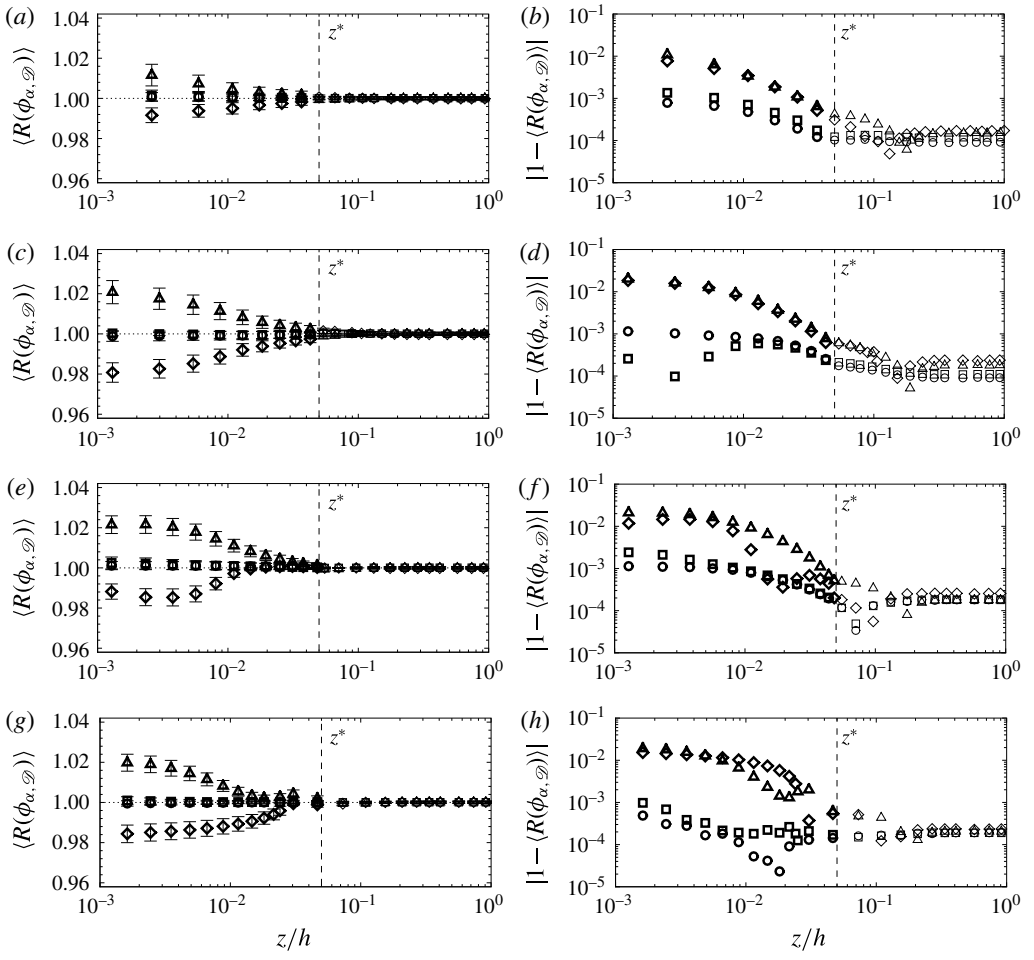


FIGURE 13. (a,c,e,g) Time-averaged renormalization functions, $\langle R(\phi_{\alpha,\mathscr{D}})\rangle$, and ($b$,$d$,$f$,$h$) deviations of $\langle R(\phi_{\alpha,\mathscr{D}})\rangle$ from unity, from nested-LES of equilibrium turbulent channel flow at (a,b) $Re_\tau \approx 1000$, (c,d) $Re_\tau \approx 2000$, (e,f) $Re_\tau \approx 5000$, (g,h) $Re_\tau \approx 10\,000$: ○, $R(\langle\langle \overline{u}_{\mathscr{D}}\rangle\langle \overline{u}_{\mathscr{D}}\rangle\rangle)$; □, $R(\langle\langle \overline{u}''_{\mathscr{D}}\overline{u}''_{\mathscr{D}}\rangle\rangle)$; ◇, $R(\langle\langle \overline{v}''_{\mathscr{D}}\overline{v}''_{\mathscr{D}}\rangle\rangle)$; △, $R(\langle\langle \overline{w}''_{\mathscr{D}}\overline{w}''_{\mathscr{D}}\rangle\rangle)$; the error bars in ($a$,$c$,$e$,$g$) show ± one standard deviation in time.

Figure 13 shows the profiles of the time-averaged renormalization functions, $\langle R(\phi_{\alpha,\mathscr{D}})\rangle$, along with the absolute magnitudes of $|1-\langle R(\phi_{\alpha,\mathscr{D}})\rangle|$, from nested-LES of turbulent channel flow at $1000 \leqslant Re_\tau \leqslant 10\,000$. In all cases, the time-averaged renormalization functions, $\langle R(\phi_{\alpha,\mathscr{D}})\rangle$, remain close to unity and stay confined to 1 ± 0.025 for $0 \leqslant z/h < 0.02$; 1 ± 0.005 for $0.02 \leqslant z/h < 0.05$; and 1 ± 0.001 for $0.05 \leqslant z/h \leqslant 1$. The main effect of $R(\phi_{\alpha,\mathscr{D}})$ in the inner layer ($z \leqslant z^*$) is to enhance the wall-normal turbulence intensities in the full domain by 0.1–2.5 %, while attenuating the spanwise turbulence intensities by 0.1–2.5 % on average at each time step. In addition, the streamwise turbulence intensities and the mean streamwise velocity are attenuated in the inner layer of the full domain by 0.05–0.5 % on average at each time step. In the outer layer ($z > z^*$), the main effect of $R(\phi_{\alpha,\mathscr{D}})$ is to attenuate the wall-normal turbulence intensities in the minimal flow unit by less than 0.1 %, while enhancing the

https://doi.org/10.1017/jfm.2016.137 Published online by Cambridge University Press

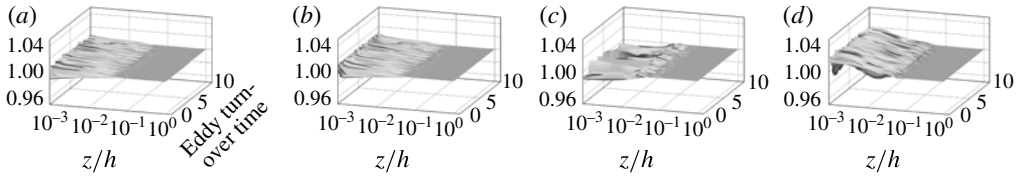


FIGURE 14. Time history of the instantaneous renormalization functions, $R(\phi_{\alpha,\mathscr{D}})$, at wall-normal locations $10^{-3} \leqslant z/h \leqslant 1.0$, from nested-LES of equilibrium turbulent channel flow at $Re_\tau \approx 10\,000$. (*a*) $R(\langle\langle \overline{u}_{\mathscr{D}} \rangle\rangle \langle\langle \overline{u}_{\mathscr{D}} \rangle\rangle)$, (*b*) $R(\langle\langle \overline{u}''_{\mathscr{D}} \overline{u}''_{\mathscr{D}} \rangle\rangle)$, (*c*) $R(\langle\langle \overline{v}''_{\mathscr{D}} \overline{v}''_{\mathscr{D}} \rangle\rangle)$, (*d*) $R(\langle\langle \overline{w}''_{\mathscr{D}} \overline{w}''_{\mathscr{D}} \rangle\rangle)$.

streamwise and spanwise turbulence intensities by less than 0.1 % and the streamwise mean velocity by less than 0.05 % on average at each time step. These small corrections, when applied at every time step, are sufficient to correct the velocity fields, spectra and turbulence statistics in both the full domain and minimal flow unit of the nested-LES approach.

Figure 14 shows the time histories of the instantaneous renormalization functions, $R(\langle\langle \overline{u}_{\alpha,\mathscr{D}} \rangle\rangle \langle\langle \overline{u}_{\alpha,\mathscr{D}} \rangle\rangle)$ and $R(\langle\langle \overline{u}''_{\alpha,\mathscr{D}} \overline{u}''_{\alpha,\mathscr{D}} \rangle\rangle)$, for the 'mean' and fluctuating components of the velocity, respectively, from nested-LES of turbulent channel flow at $Re_\tau \approx 10\,000$. Similar features are observed at other Reynolds numbers. At all Reynolds numbers, $R(\phi_{\alpha,\mathscr{D}})$ remain close to unity for $z/h \geqslant 0.05$, while fluctuating within 1 ± 0.01 for $R(\langle\langle \overline{u}_{\mathscr{D}} \rangle\rangle \langle\langle \overline{u}_{\mathscr{D}} \rangle\rangle)$ and $R(\langle\langle \overline{u}''_{\mathscr{D}} \overline{u}''_{\mathscr{D}} \rangle\rangle)$, and within 1 ± 0.03 for $R(\langle\langle \overline{v}''_{\mathscr{D}} \overline{v}''_{\mathscr{D}} \rangle\rangle)$ and $R(\langle\langle \overline{w}''_{\mathscr{D}} \overline{w}''_{\mathscr{D}} \rangle\rangle)$ for $z/h < 0.05$, with the maximum variations occurring close to the wall. When the nested-LES is started from the initial velocity field, the renormalization functions quickly converge to the range above, and no clipping or damping is needed to maintain the stability of the simulations. During the course of the simulations, the values of $R(\phi_{\alpha,\mathscr{D}})$ at a given z-location occasionally cross unity, meaning that a given component of velocity at a given location can alternate between being instantaneously amplified or attenuated. The variations in the renormalization functions with time reflect the deviations of the single-time statistics, used in the decomposition and renormalization procedures of nested-LES, from converged statistics. The moderate level of time variations in the renormalization functions indicates the presence of some level of statistical convergence in the single-time ensembles used in the decomposition and renormalization procedures of nested-LES, while not overwhelming the instantaneous dynamics of turbulence.

4.7. *Comparison to non-nested LES*

To better understand the mechanisms behind the performance of the nested-LES approach, the simulations at $Re_\tau \approx 2000$ were repeated as non-nested LES in channels with the same domain sizes and grid resolutions as those employed in the full domain and minimal flow unit of nested-LES. These cases are denoted by 2000^F and 2000^M in tables 1 and 3.

The skin friction coefficients predicted in these non-nested LES cases had errors of 31.2 % and 21.6 %, for cases 2000^F and 2000^M, respectively, compared to Dean's correlation, as shown in table 3. These errors should be contrasted with the error of 2.9 % in the prediction of C_f by nested-LES approach at the same Reynolds number, with the same domain sizes and grid spacings. The source of the large errors in C_f for case 2000^F is lack of adequate resolution in the near-wall region, while for case 2000^M, the large errors in C_f arise from the lack of adequate domain size in the outer

https://doi.org/10.1017/jfm.2016.137 Published online by Cambridge University Press

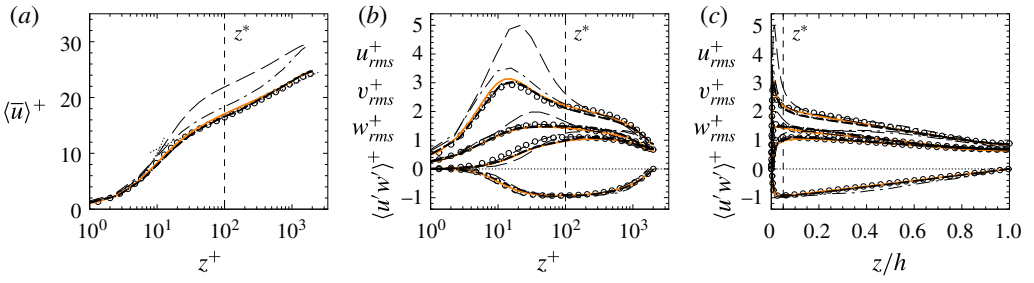


FIGURE 15. Profiles of the mean velocity, turbulence intensities and Reynolds shear stress predicted by nested-LES and non-nested LES in equilibrium turbulent channel flow at $Re_\tau \approx 2000$; – – –, full domain of nested-LES (case 2000); – · –, minimal flow unit of nested-LES (case 2000); — —, non-nested LES in full domain (case 2000^F); — · —, non-nested LES in minimal flow unit (case 2000^M); —— (orange), resolved conventional LES in full domain (case $2000^{F,h}$); ○, DNS at $Re_\tau \approx 2000$ (Hoyas & Jimenez 2006).

layer. These errors point to the need for two-way coupling in nested-LES. Clearly, the errors in C_f of non-nested cases can be reduced by performing well-resolved non-nested, conventional LES in the full-size domain, as shown by the case $2000^{F,h}$ in table 3. But such computations require $O(256^3)$ grid points compared to $O(64^3)$ of nested-LES.

The one-point turbulence statistics predicted by these non-nested LES cases also show poor agreement with DNS and resolved conventional LES, as shown in figure 15. For case 2000^F, the mean velocity profile is overpredicted throughout the cross-section of the channel and there is significant pileup of the turbulence kinetic energy near the peaks of the streamwise and spanwise turbulence intensities, which is accompanied by underprediction of the wall-normal turbulence intensity. This pileup of streamwise turbulence kinetic energy can be attributed to the lack of adequate grid resolution in case 2000^F in the inner layer, needed to resolve the pressure–strain correlations, which are responsible for redistribution of the turbulence kinetic energy from the streamwise to cross-stream directions. For case 2000^M, the mean velocity profile exhibits an upward shift of the logarithmic layer and an excessive wake region. At the same time, the peak of the streamwise turbulence intensity is overpredicted in the inner layer, and the turbulence intensities are excessively isotropic in the outer layer. The latter feature is caused by the minimal size of the computational domain, which prevents the large scales from developing into their natural anisotropic states. All these problems are resolved when the nested-LES approach is used. Figure 15 shows the turbulence statistics obtained from both the full domain and minimal flow unit of nested-LES. The differences between the two sets of turbulence statistics are hardly noticeable, reflecting the near unity values of $R(\phi_{\alpha,\mathscr{D}})$ in (2.4).

The key to the performance of the nested-LES approach can be understood by comparing the kinetic energy spectra obtained from nested-LES at $Re_\tau \approx 2000$ to the non-nested LES cases of 2000^F and 2000^M. Figure 16 shows the normalized 1-D energy spectra of the components of the fluctuating velocity in these simulations in the outer layer ($z/h \approx 0.5$) and the near-wall region ($z^+ \approx 20$), compared to the DNS data of Hoyas & Jimenez (2006). In the outer layer (figure 16*a*,*b*), both the full domain of nested-LES and the non-nested LES case of 2000^F predict spectra in good agreement with DNS, with nested-LES showing slightly better agreement with DNS than case 2000^F. The good agreement between the spectra from case 2000^F and DNS in the

https://doi.org/10.1017/jfm.2016.137 Published online by Cambridge University Press

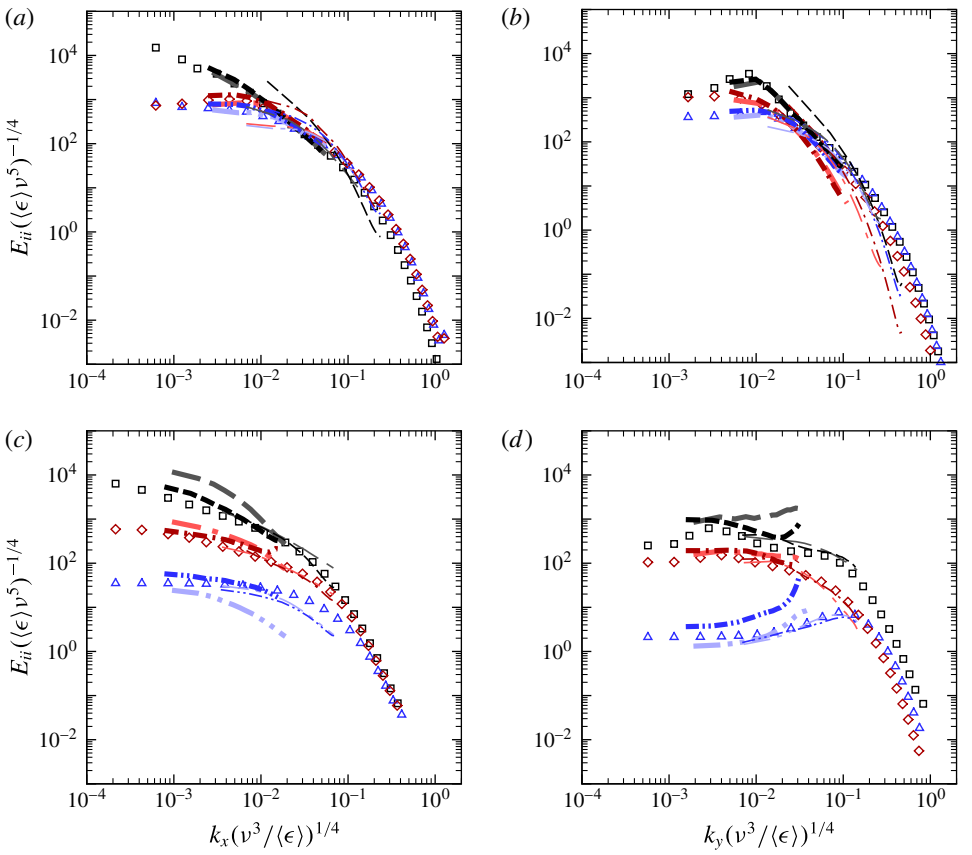


FIGURE 16. One-dimensional energy spectra of the streamwise (E_{uu}), spanwise (E_{vv}) and wall-normal (E_{ww}) velocity fluctuations, predicted by nested-LES and non-nested LES in equilibrium turbulent channel flow at $Re_\tau \approx 2000$ in (*a*,*b*) outer region ($z/h \approx 0.5$), (*c*,*d*) near-wall region ($z^+ \approx 20$): (*a*,*c*), energy spectra in the streamwise direction; (*b*,*d*), energy spectra in the spanwise direction. – – – (black, thick lines), –·– (dark red, thick lines), –··– (dark blue, thick lines): E_{uu}, E_{vv}, E_{ww}, respectively, from full domain of nested-LES (case 2000); – – – (black, thin lines), –·– (dark red, thin lines), –··– (dark blue, thin lines): E_{uu}, E_{vv}, E_{ww}, respectively, from minimal flow unit of nested-LES (case 2000); — — (grey, thick lines), — · — (light red, thick lines), —··— (light blue, thick lines): E_{uu}, E_{vv}, E_{ww}, respectively, from non-nested LES in full domain (case 2000^F); — — (grey, thin lines), — · — (light red, thin lines), —··— (light blue, thin lines): E_{uu}, E_{vv}, E_{ww}, respectively, from non-nested LES in minimal flow unit (case 2000^M); □ (black), ◇ (red), △ (blue), E_{uu}, E_{vv}, E_{ww}, respectively, from DNS at $Re_\tau \approx 2000$ (Hoyas & Jimenez 2006).

outer layer justifies using the full-domain solution as the basis of renormalization of the velocity field in the outer layer in the nested-LES approach. The non-nested LES case of 2000^M, however, predicts spectra in the outer layer which are in poor agreement with DNS. The minimal size of the domain, in this case, is not sufficient to accommodate the large-scale structures in the outer layer, and results in spectra for case 2000^M which prematurely approach the large-scale behaviour and become 'flat' in the inertial range. The two-way coupling between the minimal flow unit and the full

https://doi.org/10.1017/jfm.2016.137 Published online by Cambridge University Press

domain in nested-LES alleviates these problems, and brings the spectra in the large scales of the minimal flow unit of nested-LES closer to inertial range behaviour and DNS results. In the formulation of nested-LES, only the 'magnitudes' of the kinetic energies of the components of turbulent velocity fluctuations are rescaled at each wall-normal location, without any explicit modifications to the spectral distributions of the kinetic energies in the wall-parallel directions. Nonetheless, in practice, the renormalization procedure also corrects the 'shape' of the spectra during the course of the simulation, thus restoring both the large-scale anisotropy in the outer layer of the minimal flow unit based on results from the full domain of nested-LES, and correcting the energy cascade in the outer layer of the minimal flow unit.

Similarly, in the near-wall region (figure 16*c*,*d*), both the minimal flow unit of nested-LES and the non-nested LES case of 2000^M predict spectra in agreement with DNS. This justifies using the LES solution from the minimal flow unit as the basis of renormalization of the velocity field in the inner layer in the nested-LES approach. The non-nested LES case of 2000^F, however, predicts spectra which are in poor agreement with DNS in the near-wall region. The spectra of the streamwise and spanwise velocity fluctuations are overpredicted, while those of the wall-normal velocity fluctuations are underpredicted, for case 2000^F, consistent with the trends observed in the turbulence intensities in figure 15(*b*). The renormalization procedure in nested-LES alleviates these problems, and brings both the magnitudes and distributions of the full-domain spectra of nested-LES in closer agreement to DNS results in the inner layer. The renormalization procedure in this case, in essence, compensates for the under-resolved pressure–strain correlations in the coarse-resolution full domain, thus correcting the full-domain solution of nested-LES in the inner layer.

5. Results in non-equilibrium, strained turbulent channel flow

As a further test of the nested-LES approach, its performance was assessed in non-equilibrium turbulent channel flow. These studies were designed to emulate the experimental conditions of Driver & Hebbar (1991), as described in § 3.2. To compare the evolution of the statistics between the experiments and simulations, the skin friction coefficients and the one-point turbulence statistics, which were normalized using the free-stream velocity, U_∞, in the TBL, were normalized using the mean centreline velocity in the base equilibrium turbulent channel flow, U_c, in the simulations, as discussed in § 3.2. The evolution of all quantities was tracked as a function of $x^* = (x - x_0)/\delta_0$, where x_0 and δ_0 denote the x-location and boundary layer thickness at the end of the straining zone in the experiments, respectively, and the 'time' in the simulations was converted to 'position' in experiments using Taylor's hypothesis (see § 3.2) as $t^* = x^* = (t - t_0)(U_c/h)(\delta(x))/\delta_0$, where t_0 is the time when the spanwise straining is ceased in the simulations.

5.1. *Evolution of the skin friction coefficient*

Figure 17(*a*,*b*) show the evolution of the streamwise and spanwise skin friction coefficients, $C_{f,x}$ and $C_{f,y}$, predicted in nested-LES, compared to experimental measurements of Driver & Hebbar (1991). In the straining zone, the $C_{f,x}$ predicted by nested-LES experiences an initial drop of $\approx 20\,\%$ from its value in the base equilibrium flow, followed by recovery to a value $\approx 20\,\%$ higher than that in the base equilibrium flow, while $C_{f,y}$ rapidly settles to a magnitude comparable to $C_{f,x}$. While no experimental measurements of $C_{f,x}$ and $C_{f,y}$ are available in the straining zone, the features observed in nested-LES are similar to those reported in previous DNS

https://doi.org/10.1017/jfm.2016.137 Published online by Cambridge University Press

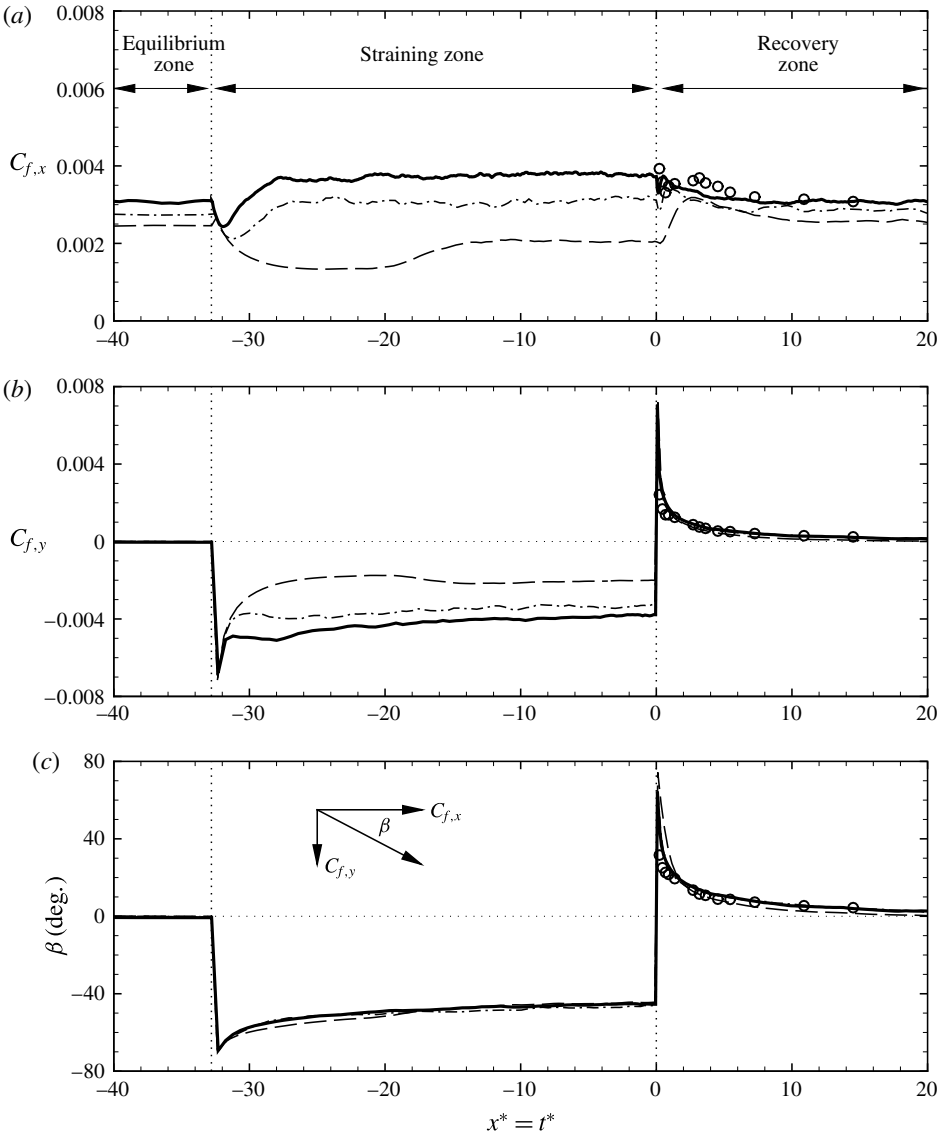


FIGURE 17. Evolution of (*a*) streamwise skin friction coefficient, $C_{f,x}$, (*b*) spanwise skin friction coefficient, $C_{f,y}$, (*c*) surface-flow angle, β, predicted by nested-LES and non-nested LES in non-equilibrium, strained turbulent channel flow, compared to experiments (Driver & Hebbar 1991). ——, nested-LES, case 2000-*S*; – – –, non-nested LES, case 2000-S^F; – · –, non-nested LES, case 2000-S^M; ○, experiments of Driver & Hebbar (1991).

studies of strained turbulent channel flow (Coleman, Kim & Le 1996), and LES of 3-D shear-driven TBL flow (Kannepalli & Piomelli 2000) at lower Reynolds numbers.

In the recovery zone, the $C_{f,x}$ predicted by nested-LES experiences a rapid drop of $\approx 10\,\%$ for $0 \leqslant x^* \lesssim 0.5$, followed by more gradual decay towards its base equilibrium channel value, while $C_{f,y}$ exhibits an exponential decay towards zero. Good overall agreement is observed between the $C_{f,x}$ and $C_{f,y}$ predicted by nested-LES and experimental data. However, the initial rapid drop of $C_{f,x}$ in the recovery region

https://doi.org/10.1017/jfm.2016.137 Published online by Cambridge University Press

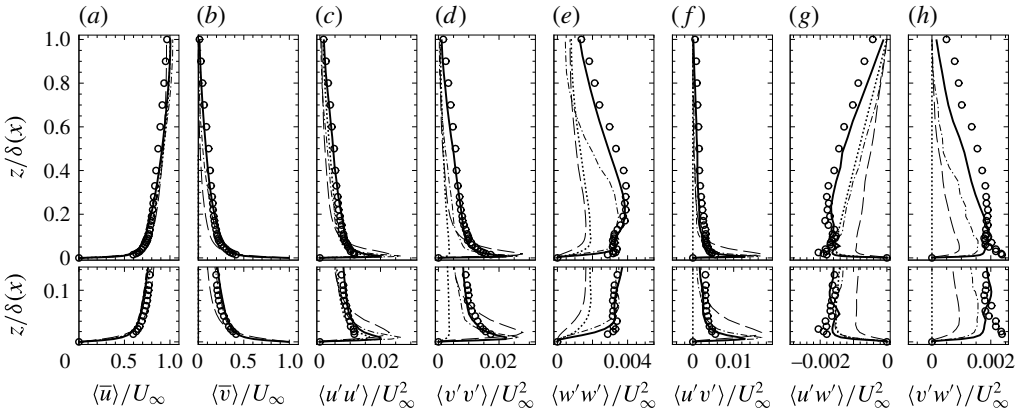


FIGURE 18. Profiles of the mean velocities and turbulent stresses at $x^* \approx -0.11$, near the end of the straining zone, predicted by nested-LES and non-nested LES in shear driven, strained turbulent channel flow, compared to experimental measurements in shear driven, three-dimensional TBL (Driver & Hebbar 1991). ——, nested-LES, case 2000-S; – – –, non-nested LES, case 2000-S^F; – · –, non-nested LES, case 2000-S^M; · · · · · ·, nested-LES in equilibrium turbulent channel flow at $Re_\tau \approx 2000$; ○, experimental data of Driver & Hebbar (1991). An enlarged view of the near-wall region is shown below each figure.

predicted by nested-LES occurs faster than experiments. This difference can be attributed to the more abrupt cessation of the transverse motion of the wall in the simulations compared to experiments.

In contrast, the non-nested LES case of 2000-S^F exhibits significant lag in response to both the impulsive start and cessation of straining, and significantly underpredicts the magnitudes of $C_{f,x}$ and $C_{f,y}$. The non-nested LES case of 2000-S^M predicts the evolution of $C_{f,x}$ and $C_{f,y}$ with features similar to those in nested-LES, but underpredicts the $C_{f,x}$ and $C_{f,y}$ by 10–15 %.

Figure 17(*c*) shows the evolution of the surface flow angle on the moving wall, defined as $\beta \equiv \tan^{-1}(C_{f,y}/C_{f,x})$. Nearly identical surface flow angles are predicted by nested-LES and non-nested LES cases of 2000-S^F and 2000-S^M, all showing good agreement with experimental data in the recovery zone. The largest discrepancies from experiments are seen for case 2000-S^F.

5.2. *Evolution of one-point turbulence statistics*

Figure 18 shows the profiles of the mean velocities and turbulent stresses predicted by the simulations, compared to experiments (Driver & Hebbar 1991), at $x^* \approx -0.11$, near the end of the straining zone. The mean spanwise velocity, $\langle \overline{v} \rangle$, develops a profile which approximately satisfies $\langle \overline{v} \rangle / V_s = 1 - \langle \overline{u} \rangle / U_\infty$, as shown in figure 19. The presence of this mean spanwise velocity leads to significant enhancement of all components of turbulent stresses in the strained flow compared to the base equilibrium flow, while the reorientation of the flow gives rise to non-zero Reynolds stresses $\langle u'v' \rangle$ and $\langle v'w' \rangle$, as seen in figure 18(*c–h*). All these predictions of nested-LES in the straining zone are in agreement with experimental data. The biggest discrepancy between experiments and nested-LES results is observed in the profile of $\langle v'w' \rangle$ at $x^* \approx -0.11$ (figure 18*h*), where experimental data show features which are characteristic of the recovery zone, $x^* \geqslant 0$. In contrast, the non-nested LES case

https://doi.org/10.1017/jfm.2016.137 Published online by Cambridge University Press

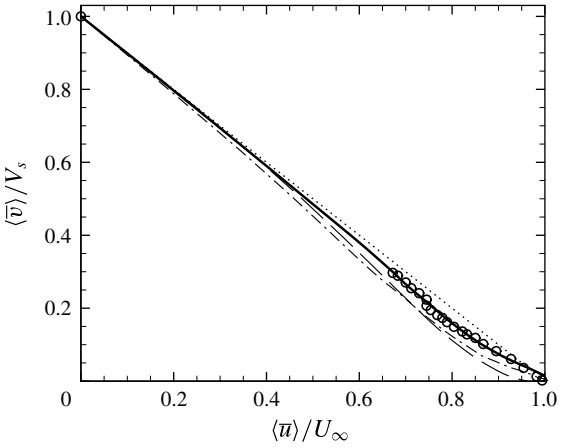


FIGURE 19. Hodograph of the mean streamwise and spanwise velocities at $x^* \approx -0.11$, near the end of the straining zone, predicted by nested-LES and non-nested LES, compared to experiments (Driver & Hebbar 1991). ——, nested-LES, case 2000-S; – – –, non-nested LES, case 2000-S^F; – · –, non-nested LES, case 2000-S^M; ○, experiments of Driver & Hebbar (1991); · · · ·, analytical expression $\langle\overline{u}\rangle/U_\infty + \langle\overline{v}\rangle/V_s = 1$.

of 2000-S^F gives inaccurate predictions for all turbulent stresses as well as the mean spanwise velocity in both the inner and outer layers, while the non-nested LES case of 2000-S^M gives acceptable results in the inner layer but predicts inaccurate turbulent stresses in the outer layer.

Figure 20(*a–h*) show the evolution of the profiles of mean velocities and turbulent stresses predicted by nested-LES at $x^* \approx 0.23$, in the initial recovery zone. In this zone, the effect of the abrupt cessation of the transverse motion of the wall remains confined to the near-wall region, and is most dramatically felt in the spanwise component of the velocity. Both $\langle\overline{v}\rangle$ and $\langle v'v'\rangle$ rapidly decay during this phase, while $\langle v'w'\rangle$ and $\langle u'v'\rangle$ develop negative peaks in the immediate vicinity of the wall. Interestingly, the near-wall peak of $\langle u'u'\rangle$ drops to 70 % of its value in the base equilibrium flow before recovery, which has also been observed in earlier numerical studies (Coleman *et al.* 1996; Kannepalli & Piomelli 2000). The nested-LES approach successfully captures all these features in agreement with experimental data. In contrast, the non-nested LES case of 2000-S^F exhibits significant lag in response to cessation of the transverse strain and fails to correctly predict any of the turbulent stresses or the mean spanwise velocity, while the non-nested LES case of 2000-S^M predicts the turbulent stresses inaccurately in the outer layer.

Figure 20(*i–p*) show the evolution of the profiles of the mean velocities and turbulent stresses predicted by nested-LES at $x^* \approx 0.9$, in the mid-recovery zone. In this zone, the effect of cessation of straining begins to penetrate into the outer layer, and the profiles of all components of the Reynolds stresses continue to decay or recover towards their equilibrium states. The nested-LES approach successfully captures the flow features in this mid-recovery zone in agreement with experimental data. The biggest discrepancy is observed in the profiles of $\langle w'w'\rangle$ and $\langle v'w'\rangle$, for which nested-LES predicts a faster decay compared to experiments. These discrepancies may be attributed to the larger spanwise and wall-normal turbulence intensities in the outer layer of TBL compared to channel flow (Jimenez *et al.* 2010).

https://doi.org/10.1017/jfm.2016.137 Published online by Cambridge University Press

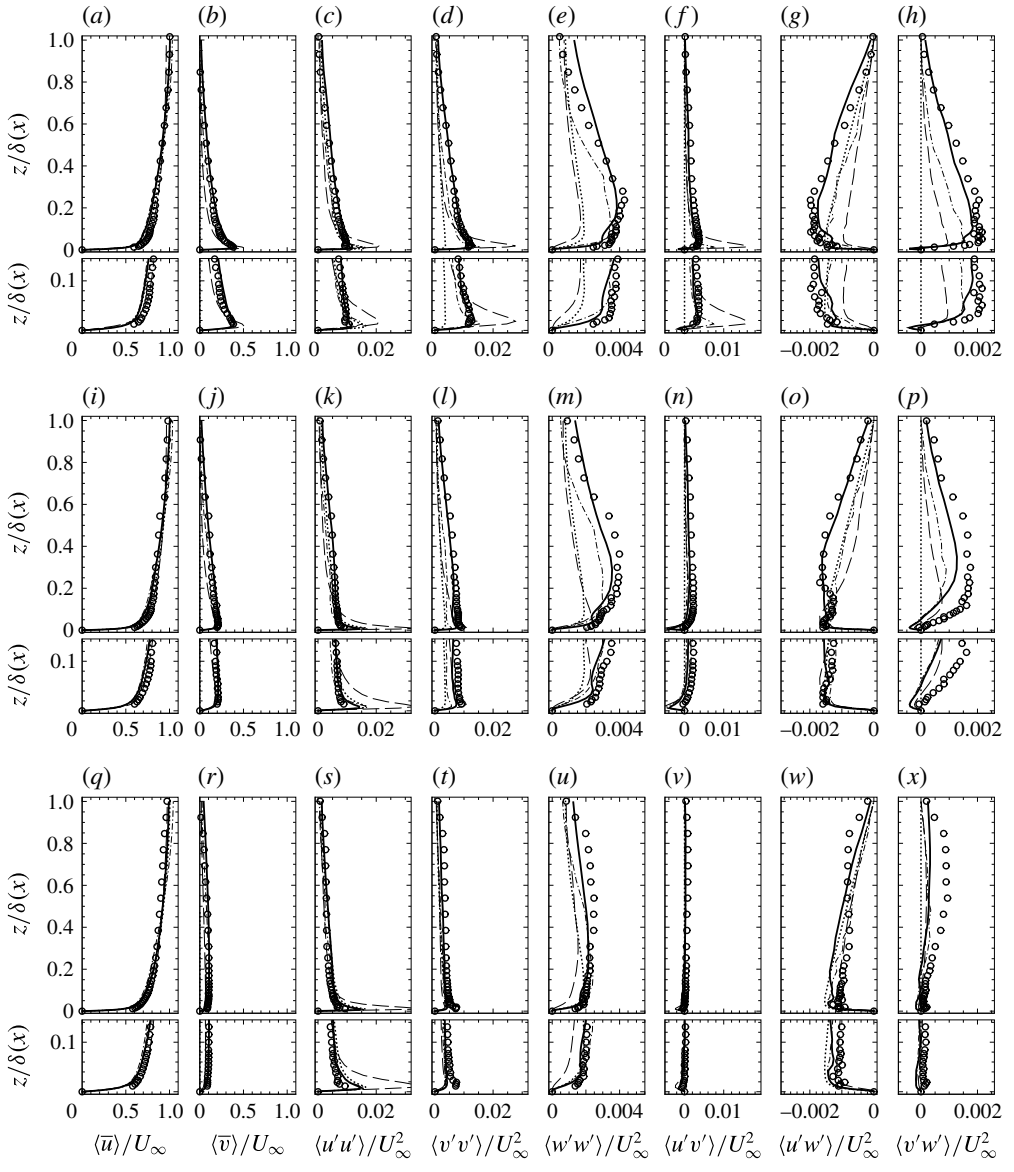


FIGURE 20. Profiles of the mean velocities and turbulent stresses predicted by nested-LES and non-nested LES in shear driven, strained turbulent channel flow, compared to experimental measurements in shear driven, three-dimensional TBL (Driver & Hebbar 1991) in (*a–h*) the initial recovery zone, $x^* \approx 0.23$, (*i–p*) the mid-recovery zone, $x^* \approx 0.91$, (*q–x*) final recovery zone, $x^* \approx 10.9$. Symbols and line types as in figure 18.

Figure 20(*q–x*) show the evolution of the profiles of the mean velocities and turbulent stresses predicted by nested-LES at $x^* \approx 10.9$, in the final recovery zone. In this zone, all turbulence statistics are approaching their equilibrium states and the predictions of nested-LES show good agreement with experimental data, except for the discrepancy in the recovery of $\langle w'w' \rangle$, $\langle v'w' \rangle$, and $\langle u'w' \rangle$ in the outer layer, which can be attributed to the same reason noted before in the mid-recovery zone.

https://doi.org/10.1017/jfm.2016.137 Published online by Cambridge University Press

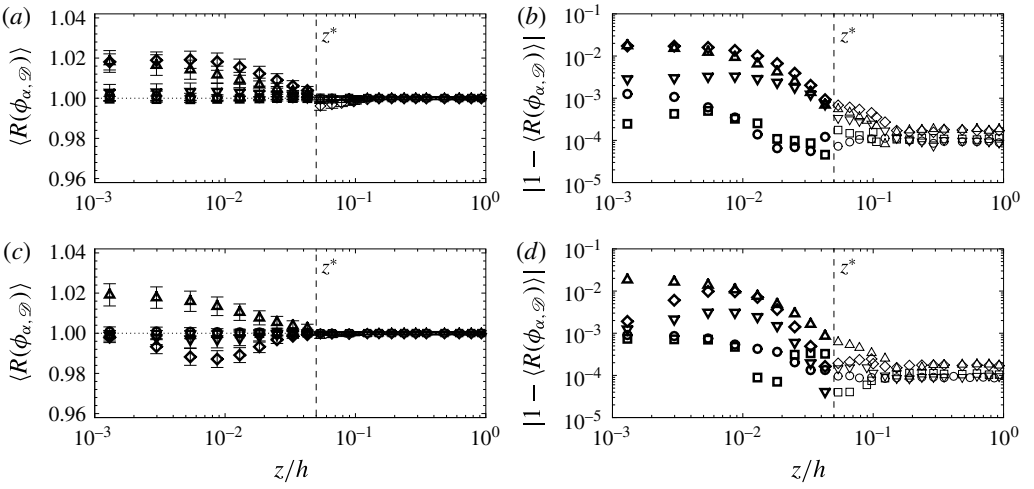


FIGURE 21. (*a*,*c*) Time-averaged renormalization functions, $\langle R(\phi_{\alpha,\mathscr{D}})\rangle$, and (*b*,*d*) deviations of $\langle R(\phi_{\alpha,\mathscr{D}})\rangle$ from unity, from nested-LES of non-equilibrium, strained turbulent channel flow in (*a*,*b*) the straining zone, and (*c*,*d*) the recovery zone: $\triangledown$, $R(\langle\!\langle\overline{v}_{\mathscr{D}}\rangle\!\rangle\langle\!\langle\overline{v}_{\mathscr{D}}\rangle\!\rangle)$; other symbols as in figure 13.

5.3. *Renormalization functions*

Figure 21 shows the profiles of the time-averaged renormalization functions, $\langle R(\phi_{\alpha,\mathscr{D}})\rangle$, and the deviations of $\langle R(\phi_{\alpha,\mathscr{D}})\rangle$ from unity, $|1-\langle R(\phi_{\alpha,\mathscr{D}})\rangle|$, observed in nested-LES of strained turbulent channel flow. Throughout the straining and recovery zones, the time-averaged renormalization functions, $\langle R(\phi_{\alpha,\mathscr{D}})\rangle$, remain confined to 1 ± 0.03 for $0\leqslant z/h<0.05$, and 1 ± 0.001 for $0.05\leqslant z/h\leqslant1$. In the recovery zone (figure 21*c*,*d*), the trends in $\langle R(\phi_{\alpha,\mathscr{D}})\rangle$ remain close to those observed in equilibrium turbulent channel, except that $R(\langle\!\langle\overline{v}''_{\mathscr{D}}\overline{v}''_{\mathscr{D}}\rangle\!\rangle)$ is closer to unity in the near-wall region and has less fluctuation. In the straining zone (figure 21*a*,*b*), the renormalization functions act to enhance the turbulence kinetic energy of $\langle\!\langle\overline{v}_{\mathscr{D}}\rangle\!\rangle$ and $\overline{v}''_{\mathscr{D}}$ by up to 0.5 % and 2 %, respectively, as required by the flow, instead of attenuating them, demonstrating the robustness of the nested-LES approach and its ability to adjust to different flow conditions.

6. Application to more complex geometries and computational savings

In the present study, the nested-LES approach has been applied to homogeneous turbulent channel flow, for which two directions of global homogeneity exist. However, the method is more general, and can be applied to any flows with at least one direction of global or local homogeneity.

In flows with two globally homogeneous (or nearly homogeneous) directions, the required number of grid points in the homogeneous directions is independent of Reynolds number for any given geometry, while the required number of grid points in the wall-normal direction has a weak Reynolds number dependence. To estimate this dependence, we note that the size of the turbulence structures is nearly fixed in outer scaling for $z/\delta>0.1$, as shown in figure 10, rendering the required number of grid points in this region independent of Reynolds number for any given geometry. In

https://doi.org/10.1017/jfm.2016.137 Published online by Cambridge University Press

the inner layer ($z/\delta < 0.1$), however, the size of the grid in the wall-normal direction needs to grow proportional to the distance from the wall, mimicking the growth in the size of the turbulence structures in this region (see figure 10). With such a grid distribution, the total number of required grid points in a slab of thickness $\mathrm{d}z$ is given by $\mathrm{d}N_{tot} \sim (N_x \cdot N_y) \cdot \mathrm{d}N_z \sim (N_x \cdot N_y) \cdot \mathrm{d}z/z$ (Jimenez 2003), where $N_x \cdot N_y$ is the required number of grid points in the homogeneous flow directions, which is independent of the Reynolds number. As such, the total number of required grid points in the whole domain grows with the Reynolds number as

$$N_{tot} \sim \int_{z_0}^{0.1\delta} \mathrm{d}z/z \sim \log(\delta/z_0) \sim \log(\delta^+/z_0^+) \sim \log(Re_\tau), \tag{6.1}$$

where z_0 is a wall-normal location corresponding to a fixed distance in wall units, z_0^+, from the wall. Thus the total number of required grid points grows weakly with the Reynolds number as $O(\log Re_\tau)$.

In flows with only one homogeneous (or nearly homogeneous) direction, such as a separating turbulent boundary layer, flow in a channel expansion, flow around any two-dimensional object, or flow in the mid-section of an airplane wing, the minimal flow unit needs to span the full length of the computational domain in the inhomogeneous wall-parallel direction, but can remain 'minimal' in the homogeneous (or nearly homogeneous) flow direction. For such flows, the required number of grid points in a slab of thickness $\mathrm{d}z$ is given by $\mathrm{d}N_{tot} \sim C\delta/z \cdot N_y \cdot \mathrm{d}z/z$ (Jimenez 2003), where $C\delta$ is the size of the domain in the inhomogeneous, wall-parallel (x), flow direction, and a grid spacing proportional to the size of the turbulent eddies, which are themselves proportional to z, is assumed in the x-direction, and N_y is number of grid points in the homogeneous (or nearly homogeneous) flow direction, which is independent of Reynolds number. As such, the total number of required grid points grows with the Reynolds number as

$$N_{tot} \sim \int_{z_0}^{\delta} \delta\, \mathrm{d}z/z^2 \sim (\delta/z_0) \sim (\delta^+/z_0^+) \sim Re_\tau, \tag{6.2}$$

in any given geometry. While the $O(Re_\tau)$ grid point requirements of flows with only one direction of homogeneity is larger than $O(\log Re_\tau)$ of flows with two directions of homogeneity, it is still a significant savings compared to $O(Re_\tau^2)$ grid point requirements of conventional LES.

In more general flows, the nested-LES approach may still be applied to regions with local homogeneity (or near homogeneity) in the flow, to offer significant computational savings compared to conventional LES. In these cases, multiple minimal flow units may be introduced to represent a local ensemble of the near-wall dynamics in different regions of the full domain. Applying the same analysis above, the number of required grid points still remains $O(\log Re_\tau)$ and $O(Re_\tau)$ in regions with two or one locally homogeneous directions, respectively.

The overhead associated with the renormalization step of nested-LES is minimal, rendering the cost of nested-LES no different from the cost of non-nested LES in each of the full domain and minimal flow unit of nested-LES. These features give nested-LES the ability to provide high-fidelity predictions in a wide range of wall flows while reducing the required number of grid points from $O(Re_\tau^2)$ of conventional LES to $O(\log Re_\tau)$ to $O(Re_\tau)$.

https://doi.org/10.1017/jfm.2016.137 Published online by Cambridge University Press

7. Summary and conclusions

A new nested-LES approach for computation of high Reynolds number equilibrium and non-equilibrium wall-bounded turbulent flows is proposed. The method couples well-resolved LES in a minimal flow unit with coarse-resolution LES in the full domain to provide high-fidelity simulations of the flow in both the inner and outer layers. The coupling between the minimal flow unit and full domain of nested-LES is achieved by dynamically renormalizing the velocity fields in each domain at each time step during the course of the simulation to match the wall-normal profiles of the single-time ensemble-averaged kinetic energies of the components of mean and fluctuating velocities in both domains to those of the minimal flow unit in the inner layer, and to those of the full domain in the outer layer. This two-way coupling corrects the magnitudes and spectral distributions of kinetic energies of all velocity components in both domains, and compensates for lack of adequate resolution in the full domain in the inner layer, and inadequate size of the minimal flow unit in the outer layer. The nested-LES approach has been applied to LES of high Reynolds number equilibrium turbulent channel flow at $Re_\tau \approx 1000$, 2000, 5000 and 10 000, and non-equilibrium, strained turbulent channel flow at $Re_\tau \approx 2000$. In both flows, nested-LES predicts the friction coefficient, first- and higher-order single-point turbulence statistics, spectra and structural features in agreement with available DNS and experimental data. A unique advantage of the nested-LES approach is its ability to accurately predict the dynamics of turbulence in both the near-wall and outer regions, thus providing a method for computing very high Reynolds number complex flows where the near-wall dynamics plays a critical role. The nested-LES approach may be applied to flows which are 'globally' or 'locally' homogeneous in at least one wall-parallel direction, and reduces the required number of grid points from $O(Re_\tau^2)$ of conventional LES to $O(\log Re_\tau)$ or $O(Re_\tau)$ in flows with two or one locally or globally homogeneous directions, respectively.

Acknowledgements

This work was supported by an unrestricted grant from the Martin R. Prince Foundation, and NSF XSEDE Allocation CTS-070070. This support is gratefully acknowledged. The study has greatly benefited from suggestions by the anonymous referees. We thank the referees for this anonymous contribution.

REFERENCES

DEL ALAMO, J. C., JIMENEZ, J., ZANDONADE, P. & MOSER, R. D. 2004 Scaling of the energy spectra of turbulent channels. *J. Fluid Mech.* **500**, 135–144.

BALAKUMAR, B. J. & ADRIAN, R. J. 2007 Large- and very-large-scale motions in channel and boundary-layer flows. *Phil. Trans. R. Soc. Lond.* A **365** (1852), 665–681.

BALARAS, E., BENOCCI, C. & PIOMELLI, U. 1996 Two-layer approximate boundary conditions for large-eddy simulations. *AIAA J.* **34** (6), 1111–1119.

CABOT, W. & MOIN, P. 1999 Approximate wall boundary conditions in the large-eddy simulation of high Reynolds number flow. *Flow Turbul. Combust.* **63** (1), 269–291.

CANUTO, C., HUSSAINI, M. Y., QUARTERONI, A. & ZANG, T. A. 1988 *Spectral Methods in Fluid Dynamics*. Springer.

CHAPMAN, D. R. 1979 Computational aerodynamics, development and outlook. *AIAA J.* **17** (12), 1293–1313.

CHUNG, D. & PULLIN, D. I. 2009 Large-eddy simulation and wall modelling of turbulent channel flow. *J. Fluid Mech.* **631**, 281–309.

https://doi.org/10.1017/jfm.2016.137 Published online by Cambridge University Press

COLEMAN, G. N., KIM, J. & LE, A. T. 1996 A numerical study of three-dimensional wall-bounded flows. *Intl J. Heat Fluid Flow* **17** (3), 333–342.

COMTE-BELLOT, G. 1963 Turbulent flow between two parallel walls. PhD thesis, University of Grenoble.

DEAN, R. B. 1978 Reynolds number dependence of skin friction and other bulk flow variables in two-dimensional rectangular duct flow. *Trans. ASME J. Fluids Engng* **100** (2), 215–223.

DEARDORFF, J. W. 1970 A numerical study of three-dimensional turbulent channel flow at large Reynolds numbers. *J. Fluid Mech.* **41**, 453–480.

DRIVER, D. M. & HEBBAR, S. K. 1991 Three-dimensional turbulent boundary layer flow over a spinning cylinder. *NASA Tech. Rep.* TM-102240. AMES Research Center.

FLORES, O. & JIMENEZ, J. 2010 Hierarchy of minimal flow units in the logarithmic layer. *Phys. Fluids* **22** (7), 071704.

GERMANO, M., PIOMELLI, U., MOIN, P. & CABOT, W. H. 1991 A dynamic subgrid-scale eddy viscosity model. *Phys. Fluids* A **3** (7), 1760–1765.

HALILOGLU, M. U. & AKHAVAN, R. 2004 A nonlinear interactions approximation model for LES. In *Direct and Large-Eddy Simulation V* (ed. B. Geurts, O. Metais & R. Freidrich), ERCOFTAC Series, vol. 9, p. 39. Kluwer.

HOFFMANN, G. & BENOCCI, C. 1995 Approximate wall boundary conditions for large eddy simulations. In *Advances in Turbulence V* (ed. R. Benzi), pp. 222–228. Kluwer.

HOYAS, S. & JIMENEZ, J. 2006 Scaling of the velocity fluctuations in turbulent channels up to $Re_\tau = 2003$. *Phys. Fluids* **18** (1), 011702.

HULTMARK, M., VALLIKIVI, M., BAILEY, S. C. C. & SMITS, A. J. 2013 Logarithmic scaling of turbulence in smooth- and rough-wall pipe flow. *J. Fluid Mech.* **728**, 376–395.

HUTCHINS, N. & MARUSIC, I. 2007 Large-scale influences in near-wall turbulence. *Phil. Trans. R. Soc. Lond.* A **365** (1852), 647–664.

HWANG, Y. Y. 2013 Near-wall turbulent fluctuations in the absence of wide outer motions. *J. Fluid Mech.* **723**, 264–288.

JIMENEZ, J. 2003 Computing high-Reynolds-number turbulence: will simulations ever replace experiments? *J. Turbul.* **4**, N22.

JIMENEZ, J. & HOYAS, S. 2008 Turbulent fluctuations above the buffer layer of wall-bounded flows. *J. Fluid Mech.* **611**, 215–236.

JIMENEZ, J., HOYAS, S., SIMENS, M. P. & MIZUNO, Y. 2010 Turbulent boundary layers and channels at moderate Reynolds numbers. *J. Fluid Mech.* **657**, 335–360.

JIMENEZ, J. & MOIN, P. 1991 The minimal flow unit in near-wall turbulence. *J. Fluid Mech.* **225**, 213–240.

KANNEPALLI, C. & PIOMELLI, U. 2000 Large-eddy simulation of a three-dimensional shear-driven turbulent boundary layer. *J. Fluid Mech.* **423**, 175–203.

KEMENOV, K. & MENON, S. 2003 Two level simulation of high-Reynolds number non-homogeneous turbulent flows. *AIAA Paper* 2003-0084.

KNAEPEN, B., DEBLIQUY, O. & CARATI, D. 2002 Subgrid-scale energy and pseudo pressure in large-eddy simulation. *Phys. Fluids* **14** (12), 4235–4241.

KOSLOFF, D. & TALEZER, H. 1993 A modified Chebyshev pseudospectral method with an $O(1/N)$ time step restriction. *J. Comput. Phys.* **104** (2), 457–469.

KRAVCHENKO, A. G., MOIN, P. & MOSER, R. 1996 Zonal embedded grids for numerical simulations of wall-bounded turbulent flows. *J. Comput. Phys.* **127** (2), 412–423.

LEE, M. & MOSER, R. D. 2015 Direct numerical simulation of turbulent channel flow up to $Re_\tau \approx 5200$. *J. Fluid Mech.* **774**, 395–415.

LILLY, D. K. 1992 A proposed modification of the Germano subgrid-scale closure method. *Phys. Fluids* A **4** (3), 633–635.

MARUSIC, I. & HEUER, W. D. C. 2007 Reynolds number invariance of the structure inclination angle in wall turbulence. *Phys. Rev. Lett.* **99** (11), 114504.

MARUSIC, I., MATHIS, R. & HUTCHINS, N. 2010*a* Predictive model for wall-bounded turbulent flow. *Science* **329** (5988), 193–196.

https://doi.org/10.1017/jfm.2016.137 Published online by Cambridge University Press

MARUSIC, I., MCKEON, B. J., MONKEWITZ, P. A., NAGIB, H. M., SMITS, A. J. & SREENIVASAN, K. R. 2010*b* Wall-bounded turbulent flows at high Reynolds numbers: recent advances and key issues. *Phys. Fluids* **22** (6), 065103.

MARUSIC, I., MONTY, J. P., HULTMARK, M. & SMITS, A. J. 2013 On the logarithmic region in wall turbulence. *J. Fluid Mech.* **716**, R3.

MATHIS, R., HUTCHINS, N. & MARUSIC, I. 2009 Large-scale amplitude modulation of the small-scale structures in turbulent boundary layers. *J. Fluid Mech.* **628**, 311–337.

MATHIS, R., HUTCHINS, N. & MARUSIC, I. 2011 A predictive inner-outer model for streamwise turbulence statistics in wall-bounded flows. *J. Fluid Mech.* **681**, 537–566.

MENEVEAU, C. & MARUSIC, I. 2013 Generalized logarithmic law for high-order moments in turbulent boundary layers. *J. Fluid Mech.* **719**, R1.

MENTER, F. R. & EGOROV, Y. 2005 A scale-adaptive simulation model using two-equation models. *AIAA Paper* 2005-1095.

MEYERS, J. & BAELMANS, M. 2004 Determination of subfilter energy in large-eddy simulations. *J. Turbul.* **5**, N26.

NIKITIN, N. V., NICOUD, F., WASISTHO, B., SQUIRES, K. D. & SPALART, P. R. 2000 An approach to wall modeling in large-eddy simulations. *Phys. Fluids* **12** (7), 1629–1632.

ORSZAG, S. A. 1980 Spectral methods for problems in complex geometries. *J. Comput. Phys.* **37** (1), 70–92.

PAO, Y. H. 1965 Structure of turbulent velocity and scalar fields at large wavenumbers. *Phys. Fluids* **8** (6), 1063–1075.

PERRY, A. E., HENBEST, S. & CHONG, M. S. 1986 A theoretical and experimental-study of wall turbulence. *J. Fluid Mech.* **165**, 163–199.

PIOMELLI, U. 2008 Wall-layer models for large-eddy simulations. *Prog. Aerosp. Sci.* **44** (6), 437–446.

POPE, S. B. 2000 *Turbulent Flows*. Cambridge University Press.

ROBINSON, S. K. 1991 Coherent motions in the turbulent boundary layer. *Annu. Rev. Fluid Mech.* **23**, 601–639.

SAGAUT, P. & DECK, S. 2009 Large eddy simulation for aerodynamics: status and perspectives. *Phil. Trans. R. Soc. Lond.* A **367** (1899), 2849–2860.

SAGAUT, P. & MENEVEAU, C. 2006 *Large Eddy Simulation for Incompressible Flows: An Introduction*, 3rd edn. Springer.

SCHLATTER, P., LI, Q., BRETHOUWER, G., JOHANSSON, A. V. & HENNINGSON, D. S. 2010 Simulations of spatially evolving turbulent boundary layers up to $Re_\theta = 4300$. *Intl J. Heat Fluid Flow* **31** (3), 251–261.

SCHUMANN, U. 1975 Subgrid scale model for finite difference simulations of turbulent flows in plane channels and annuli. *J. Comput. Phys.* **18** (4), 376–404.

SHUR, M. L., SPALART, P. R., STRELETS, M. K. & TRAVIN, A. K. 2008 A hybrid RANS-LES approach with delayed-DES and wall-modelled LES capabilities. *Intl J. Heat Fluid Flow* **29** (6), 1638–1649.

SILLERO, J. A., JIMENEZ, J. & MOSER, R. D. 2014 Two-point statistics for turbulent boundary layers and channels at Reynolds numbers up to $\delta^+ \approx 2000$. *Phys. Fluids* **26** (10), 105109.

SMITS, A. J., MCKEON, B. J. & MARUSIC, I. 2011 High-Reynolds number wall turbulence. *Annu. Rev. Fluid Mech.* **43**, 353–375.

SPALART, P. R., JOU, W.-H., STRELETS, M. & ALLMARAS, S. R. 1997 Comments on the feasibility of LES for wings, and on a hybrid RANS/LES approach. In *Advances in DNS/LES* (ed. C. Liu, Z. Liu & L. Sakell), pp. 137–147. Greyden.

STEVENS, R. J. A. M., WILCZEK, M. & MENEVEAU, C. 2014 Large-eddy simulation study of the logarithmic law for second- and higher-order moments in turbulent wall-bounded flow. *J. Fluid Mech.* **757**, 888–907.

TALLURU, K. M., BAIDYA, R., HUTCHINS, N. & MARUSIC, I. 2014 Amplitude modulation of all three velocity components in turbulent boundary layers. *J. Fluid Mech.* **746**, R1.

TANG, Y. 2015 A nested-LES approach for computation of high Reynolds number, equilibrium and non-equilibrium turbulent wall-bounded flows. PhD thesis, University of Michigan.

https://doi.org/10.1017/jfm.2016.137 Published online by Cambridge University Press

TANG, Y. & AKHAVAN, R. 2009 Recovery of subgrid-scale turbulence kinetic energy in LES of channel flow. In *Advances in Turbulence XII* (ed. B. Eckhardt), Springer Proceedings in Physics, vol. 132, p. 949. Springer.

TOWNSEND, A. A. 1958 The turbulent boundary layer. In *Boundary Layer Research* (ed. H. Görtler), pp. 1–15. Springer.

TOWNSEND, A. A. 1976 *The Structure of Turbulent Shear Flow*, 2nd edn. Cambridge University Press.

VOELKL, T., PULLIN, D. I. & CHAN, D. C. 2000 A physical-space version of the stretched-vortex subgrid-stress model for large-eddy simulation. *Phys. Fluids* **12** (7), 1810–1825.

WINCKELMANS, G. S., JEANMART, H. & CARATI, D. 2002 On the comparison of turbulence intensities from large-eddy simulation with those from experiment or direct numerical simulation. *Phys. Fluids* **14** (5), 1809–1811.

WU, Y. & CHRISTENSEN, K. T. 2010 Spatial structure of a turbulent boundary layer with irregular surface roughness. *J. Fluid Mech.* **655**, 380–418.

YAKHOT, A., ORSZAG, S. A., YAKHOT, V. & ISRAELI, M. 1989 Renormalization group formulation of large-eddy simulations. *J. Sci. Comput.* **4** (2), 139–158.

https://doi.org/10.1017/jfm.2016.137 Published online by Cambridge University Press